# Amplitude analysis and branching fraction measurement of $D_s^+ \to K^- K^+ \pi^+ \pi^0$

M. Ablikim,[1] M. N. Achasov,[10,c] P. Adlarson,[67] S. Ahmed,[15] M. Albrecht,[4] R. Aliberti,[28] A. Amoroso,[66a,66c] M. R. An,[32] Q. An,[63,49] X. H. Bai,[57] Y. Bai,[48] O. Bakina,[29] R. Baldini Ferroli,[23a] I. Balossino,[24a] Y. Ban,[38,k] K. Begzsuren,[26] N. Berger,[28] M. Bertani,[23a] D. Bettoni,[24a] F. Bianchi,[66a,66c] J. Bloms,[60] A. Bortone,[66a,66c] I. Boyko,[29] R. A. Briere,[5] H. Cai,[68] X. Cai,[1,49] A. Calcaterra,[23a] G. F. Cao,[1,54] N. Cao,[1,54] S. A. Cetin,[53a] J. F. Chang,[1,49] W. L. Chang,[1,54] G. Chelkov,[29,b] D. Y. Chen,[6] G. Chen,[1] H. S. Chen,[1,54] M. L. Chen,[1,49] S. J. Chen,[35] X. R. Chen,[25] Y. B. Chen,[1,49] Z. J. Chen,[20,l] W. S. Cheng,[66c] G. Cibinetto,[24a] F. Cossio,[66c] X. F. Cui,[36] H. L. Dai,[1,49] X. C. Dai,[1,54] A. Dbeyssi,[15] R. E. de Boer,[4] D. Dedovich,[29] Z. Y. Deng,[1] A. Denig,[28] I. Denysenko,[29] M. Destefanis,[66a,66c] F. De Mori,[66a,66c] Y. Ding,[33] C. Dong,[36] J. Dong,[1,49] L. Y. Dong,[1,54] M. Y. Dong,[1,49,54] X. Dong,[68] S. X. Du,[71] Y. L. Fan,[68] J. Fang,[1,49] S. S. Fang,[1,54] Y. Fang,[1] R. Farinelli,[24a] L. Fava,[66b,66c] F. Feldbauer,[4] G. Felici,[23a] C. Q. Feng,[63,49] J. H. Feng,[50] M. Fritsch,[4] C. D. Fu,[1] Y. Gao,[63,49] Y. Gao,[38,k] Y. Gao,[64] Y. G. Gao,[6] I. Garzia,[24a,24b] P. T. Ge,[68] C. Geng,[50] E. M. Gersabeck,[58] A. Gilman,[61] K. Goetzen,[11] L. Gong,[33] W. X. Gong,[1,49] W. Gradl,[28] M. Greco,[66a,66c] L. M. Gu,[35] M. H. Gu,[1,49] S. Gu,[2] Y. T. Gu,[13] C. Y. Guan,[1,54] A. Q. Guo,[22] L. B. Guo,[34] R. P. Guo,[40] Y. P. Guo,[9,h] A. Guskov,[29] T. T. Han,[41] W. Y. Han,[32] X. Q. Hao,[16] F. A. Harris,[56] N. Hüsken,[60] K. L. He,[1,54] F. H. Heinsius,[4] C. H. Heinz,[28] T. Held,[4] Y. K. Heng,[1,49,54] C. Herold,[51] M. Himmelreich,[11,f] T. Holtmann,[4] G. Y. Hou,[1,54] Y. R. Hou,[54] Z. L. Hou,[1] H. M. Hu,[1,54] J. F. Hu,[47,m] T. Hu,[1,49,54] Y. Hu,[1] G. S. Huang,[63,49] L. Q. Huang,[64] X. T. Huang,[41] Y. P. Huang,[1] Z. Huang,[38,k] T. Hussain,[65] W. Ikegami Andersson,[67] W. Imoehl,[22] M. Irshad,[63,49] S. Jaeger,[4] S. Janchiv,[26,j] Q. Ji,[1] Q. P. Ji,[16] X. B. Ji,[1,54] X. L. Ji,[1,49] Y. Y. Ji,[41] H. B. Jiang,[41] X. S. Jiang,[1,49,54] J. B. Jiao,[41] Z. Jiao,[18] S. Jin,[35] Y. Jin,[57] M. Q. Jing,[1,54] T. Johansson,[67] N. Kalantar-Nayestanaki,[55] X. S. Kang,[33] R. Kappert,[55] M. Kavatsyuk,[55] B. C. Ke,[43,1] I. K. Keshk,[4] A. Khoukaz,[60] P. Kiese,[28] R. Kiuchi,[1] R. Kliemt,[11] L. Koch,[30] O. B. Kolcu,[53a,e] B. Kopf,[4] M. Kuemmel,[4] M. Kuessner,[4] A. Kupsc,[67] M. G. Kurth,[1,54] W. Kühn,[30] J. J. Lane,[58] J. S. Lange,[30] P. Larin,[15] A. Lavania,[21] L. Lavezzi,[66a,66c] Z. H. Lei,[63,49] H. Leithoff,[28] M. Lellmann,[28] T. Lenz,[28] C. Li,[39] C. H. Li,[32] Cheng Li,[63,49] D. M. Li,[71] F. Li,[1,49] G. Li,[1] H. Li,[43] H. Li,[63,49] H. B. Li,[1,54] H. J. Li,[9,h] J. L. Li,[41] J. Q. Li,[4] J. S. Li,[50] Ke Li,[1] L. K. Li,[1] Lei Li,[3] P. R. Li,[31] S. Y. Li,[52] W. D. Li,[1,54] W. G. Li,[1] X. H. Li,[63,49] X. L. Li,[41] Xiaoyu Li,[1,54] Z. Y. Li,[50] H. Liang,[1,54] H. Liang,[63,49] H. Liang,[27] Y. F. Liang,[45] Y. T. Liang,[25] G. R. Liao,[12] L. Z. Liao,[1,54] J. Libby,[21] C. X. Lin,[50] B. J. Liu,[1] C. X. Liu,[1] D. Liu,[63,49] F. H. Liu,[44] Fang Liu,[1] Feng Liu,[6] H. B. Liu,[13] H. M. Liu,[1,54] Huanhuan Liu,[1] Huihui Liu,[17] J. B. Liu,[63,49] J. L. Liu,[64] J. Y. Liu,[1,54] K. Liu,[1] K. Y. Liu,[33] L. Liu,[63,49] M. H. Liu,[9,h] P. L. Liu,[1] Q. Liu,[68] Q. Liu,[54] S. B. Liu,[63,49] Shuai Liu,[46] T. Liu,[1,54] W. M. Liu,[63,49] X. Liu,[31] Y. Liu,[31] Y. B. Liu,[36] Z. A. Liu,[1,49,54] Z. Q. Liu,[41] X. C. Lou,[1,49,54] F. X. Lu,[16] F. X. Lu,[50] H. J. Lu,[18] J. D. Lu,[1,54] J. G. Lu,[1,49] X. L. Lu,[1] Y. Lu,[1] Y. P. Lu,[1,49] C. L. Luo,[34] M. X. Luo,[70] P. W. Luo,[50] T. Luo,[9,h] X. L. Luo,[1,49] S. Lusso,[66c] X. R. Lyu,[54] F. C. Ma,[33] H. L. Ma,[1] L. L. Ma,[41] M. M. Ma,[1,54] Q. M. Ma,[1] R. Q. Ma,[1,54] R. T. Ma,[54] X. X. Ma,[1,54] X. Y. Ma,[1,49] F. E. Maas,[15] M. Maggiora,[66a,66c] S. Maldaner,[4] S. Malde,[61] Q. A. Malik,[65] A. Mangoni,[23b] Y. J. Mao,[38,k] Z. P. Mao,[1] S. Marcello,[66a,66c] Z. X. Meng,[57] J. G. Messchendorp,[55] G. Mezzadri,[24a] T. J. Min,[35] R. E. Mitchell,[22] X. H. Mo,[1,49,54] Y. J. Mo,[6] N. Yu. Muchnoi,[10,c] H. Muramatsu,[59] S. Nakhoul,[11,f] Y. Nefedov,[29] F. Nerling,[11,f] I. B. Nikolaev,[10,c] Z. Ning,[1,49] S. Nisar,[8,i] S. L. Olsen,[54] Q. Ouyang,[1,49,54] S. Pacetti,[23b,23c] X. Pan,[9,h] Y. Pan,[58] A. Pathak,[1] P. Patteri,[23a] M. Pelizaeus,[4] H. P. Peng,[63,49] K. Peters,[11,f] J. Pettersson,[67] J. L. Ping,[34] R. G. Ping,[1,54] R. Poling,[59] V. Prasad,[63,49] H. Qi,[63,49] H. R. Qi,[52] K. H. Qi,[25] M. Qi,[35] T. Y. Qi,[2] T. Y. Qi,[9] S. Qian,[1,49] W. B. Qian,[54] Z. Qian,[50] C. F. Qiao,[54] L. Q. Qin,[12] X. P. Qin,[9] X. S. Qin,[41] Z. H. Qin,[1,49] J. F. Qiu,[1] S. Q. Qu,[36] K. H. Rashid,[65] K. Ravindran,[21] C. F. Redmer,[28] A. Rivetti,[66c] V. Rodin,[55] M. Rolo,[66c] G. Rong,[1,54] Ch. Rosner,[15] M. Rump,[60] H. S. Sang,[63] A. Sarantsev,[29,d] Y. Schelhaas,[28] C. Schnier,[4] K. Schoenning,[67] M. Scodeggio,[24a,24b] D. C. Shan,[46] W. Shan,[19] X. Y. Shan,[63,49] J. F. Shangguan,[46] M. Shao,[63,49] C. P. Shen,[9] H. F. Shen,[1,54] P. X. Shen,[36] X. Y. Shen,[1,54] H. C. Shi,[63,49] R. S. Shi,[1,54] X. Shi,[1,49] X. D. Shi,[63,49] J. J. Song,[41] W. M. Song,[27,1] Y. X. Song,[38,k] S. Sosio,[66a,66c] S. Spataro,[66a,66c] K. X. Su,[68] P. P. Su,[46] F. F. Sui,[41] G. X. Sun,[1] H. K. Sun,[1] J. F. Sun,[16] L. Sun,[68] S. S. Sun,[1,54] T. Sun,[1,54] W. Y. Sun,[34] W. Y. Sun,[27] X. Sun,[20,l] Y. J. Sun,[63,49] Y. K. Sun,[63,49] Y. Z. Sun,[1] Z. T. Sun,[1] Y. H. Tan,[68] Y. X. Tan,[63,49] C. J. Tang,[45] G. Y. Tang,[1] J. Tang,[50] J. X. Teng,[63,49] V. Thoren,[67] W. H. Tian,[43] I. Uman,[53b] B. Wang,[1] C. W. Wang,[35] D. Y. Wang,[38,k] H. J. Wang,[31] H. P. Wang,[1,54] K. Wang,[1,49] L. L. Wang,[1] M. Wang,[41] M. Z. Wang,[38,k] Meng Wang,[1,54] W. Wang,[50] W. H. Wang,[68] W. P. Wang,[63,49] X. Wang,[38,k] X. F. Wang,[31] X. L. Wang,[9,h] Y. Wang,[63,49] Y. Wang,[50] Y. D. Wang,[37] Y. F. Wang,[1,49,54] Y. Q. Wang,[1] Y. Y. Wang,[31] Z. Wang,[1,49] Z. Y. Wang,[1] Ziyi Wang,[54] Zongyuan Wang,[1,54] D. H. Wei,[12] P. Weidenkaff,[28] F. Weidner,[60] S. P. Wen,[1] D. J. White,[58] U. Wiedner,[4] G. Wilkinson,[61] M. Wolke,[67] L. Wollenberg,[4] J. F. Wu,[1,54] L. H. Wu,[1] L. J. Wu,[1,54] X. Wu,[9,h] Z. Wu,[1,49] L. Xia,[63,49] H. Xiao,[9,h] S. Y. Xiao,[1] Z. J. Xiao,[34] X. H. Xie,[38,k] Y. G. Xie,[1,49] Y. H. Xie,[6] T. Y. Xing,[1,54] G. F. Xu,[1] Q. J. Xu,[14] W. Xu,[1,54] X. P. Xu,[46] Y. C. Xu,[54] F. Yan,[9,h] L. Yan,[9,h] W. B. Yan,[63,49] W. C. Yan,[71] Xu Yan,[46] H. J. Yang,[42,g] H. X. Yang,[1] L. Yang,[43] S. L. Yang,[54] Y. X. Yang,[12] Yifan Yang,[1,54] Zhi Yang,[25] M. Ye,[1,49] M. H. Ye,[7] J. H. Yin,[1] Z. Y. You,[50] B. X. Yu,[1,49,54] C. X. Yu,[36] G. Yu,[1,54] J. S. Yu,[20,l] T. Yu,[64] C. Z. Yuan,[1,54] L. Yuan,[2]

X. Q. Yuan,[38,k] Y. Yuan,[1] Z. Y. Yuan,[50] C. X. Yue,[32] A. Yuncu,[53a,a] A. A. Zafar,[65] Zeng,[6] Y. Zeng,[20,l] A. Q. Zhang,[1] B. X. Zhang,[1] Guangyi Zhang,[16] H. Zhang,[63] H. H. Zhang,[50] H. H. Zhang,[27] H. Y. Zhang,[1,49] J. J. Zhang,[43] J. L. Zhang,[69] J. Q. Zhang,[34] J. W. Zhang,[1,49,54] J. Y. Zhang,[1] J. Z. Zhang,[1,54] Jianyu Zhang,[1,54] Jiawei Zhang,[1,54] L. Q. Zhang,[50] Lei Zhang,[35] S. Zhang,[50] S. F. Zhang,[35] Shulei Zhang,[20,l] X. D. Zhang,[37] X. Y. Zhang,[41] Y. Zhang,[61] Y. H. Zhang,[1,49] Y. T. Zhang,[63,49] Yan Zhang,[63,49] Yao Zhang,[1] Yi Zhang,[9,h] Z. H. Zhang,[6] Z. Y. Zhang,[68] G. Zhao,[1] J. Zhao,[32] J. Y. Zhao,[1,54] J. Z. Zhao,[1,49] Lei Zhao,[63,49] Ling Zhao,[1] M. G. Zhao,[36] Q. Zhao,[1] S. J. Zhao,[71] Y. B. Zhao,[1,49] Y. X. Zhao,[25] Z. G. Zhao,[63,49] A. Zhemchugov,[29,b] B. Zheng,[64] J. P. Zheng,[1,49] Y. Zheng,[38,k] Y. H. Zheng,[54] B. Zhong,[34] C. Zhong,[64] L. P. Zhou,[1,54] Q. Zhou,[1,54] X. Zhou,[68] X. K. Zhou,[54] X. R. Zhou,[63,49] A. N. Zhu,[1,54] J. Zhu,[36] K. Zhu,[1] K. J. Zhu,[1,49,54] S. H. Zhu,[62] T. J. Zhu,[69] W. J. Zhu,[36] W. J. Zhu,[9,h] Y. C. Zhu,[63,49] Z. A. Zhu,[1,54] B. S. Zou,[1] and J. H. Zou[1]

(BESIII Collaboration)

[1]*Institute of High Energy Physics, Beijing 100049, People's Republic of China*
[2]*Beihang University, Beijing 100191, People's Republic of China*
[3]*Beijing Institute of Petrochemical Technology, Beijing 102617, People's Republic of China*
[4]*Bochum Ruhr-University, D-44780 Bochum, Germany*
[5]*Carnegie Mellon University, Pittsburgh, Pennsylvania 15213, USA*
[6]*Central China Normal University, Wuhan 430079, People's Republic of China*
[7]*China Center of Advanced Science and Technology, Beijing 100190, People's Republic of China*
[8]*COMSATS University Islamabad, Lahore Campus, Defence Road, Off Raiwind Road, 54000 Lahore, Pakistan*
[9]*Fudan University, Shanghai 200443, People's Republic of China*
[10]*G.I. Budker Institute of Nuclear Physics SB RAS (BINP), Novosibirsk 630090, Russia*
[11]*GSI Helmholtzcentre for Heavy Ion Research GmbH, D-64291 Darmstadt, Germany*
[12]*Guangxi Normal University, Guilin 541004, People's Republic of China*
[13]*Guangxi University, Nanning 530004, People's Republic of China*
[14]*Hangzhou Normal University, Hangzhou 310036, People's Republic of China*
[15]*Helmholtz Institute Mainz, Staudinger Weg 18, D-55099 Mainz, Germany*
[16]*Henan Normal University, Xinxiang 453007, People's Republic of China*
[17]*Henan University of Science and Technology, Luoyang 471003, People's Republic of China*
[18]*Huangshan College, Huangshan 245000, People's Republic of China*
[19]*Hunan Normal University, Changsha 410081, People's Republic of China*
[20]*Hunan University, Changsha 410082, People's Republic of China*
[21]*Indian Institute of Technology Madras, Chennai 600036, India*
[22]*Indiana University, Bloomington, Indiana 47405, USA*
[23a]*INFN Laboratori Nazionali di Frascati, I-00044, Frascati, Italy*
[23b]*INFN Sezione di Perugia, I-06100, Perugia, Italy*
[23c]*University of Perugia, I-06100, Perugia, Italy*
[24a]*INFN Sezione di Ferrara, I-44122, Ferrara, Italy*
[24b]*University of Ferrara, I-44122, Ferrara, Italy*
[25]*Institute of Modern Physics, Lanzhou 730000, People's Republic of China*
[26]*Institute of Physics and Technology, Peace Avenue 54B, Ulaanbaatar 13330, Mongolia*
[27]*Jilin University, Changchun 130012, People's Republic of China*
[28]*Johannes Gutenberg University of Mainz, Johann-Joachim-Becher-Weg 45, D-55099 Mainz, Germany*
[29]*Joint Institute for Nuclear Research, 141980 Dubna, Moscow region, Russia*
[30]*Justus-Liebig-Universitaet Giessen, II. Physikalisches Institut, Heinrich-Buff-Ring 16, D-35392 Giessen, Germany*
[31]*Lanzhou University, Lanzhou 730000, People's Republic of China*
[32]*Liaoning Normal University, Dalian 116029, People's Republic of China*
[33]*Liaoning University, Shenyang 110036, People's Republic of China*
[34]*Nanjing Normal University, Nanjing 210023, People's Republic of China*
[35]*Nanjing University, Nanjing 210093, People's Republic of China*
[36]*Nankai University, Tianjin 300071, People's Republic of China*
[37]*North China Electric Power University, Beijing 102206, People's Republic of China*
[38]*Peking University, Beijing 100871, People's Republic of China*
[39]*Qufu Normal University, Qufu 273165, People's Republic of China*
[40]*Shandong Normal University, Jinan 250014, People's Republic of China*
[41]*Shandong University, Jinan 250100, People's Republic of China*
[42]*Shanghai Jiao Tong University, Shanghai 200240, People's Republic of China*

[43]Shanxi Normal University, Linfen 041004, People's Republic of China
[44]Shanxi University, Taiyuan 030006, People's Republic of China
[45]Sichuan University, Chengdu 610064, People's Republic of China
[46]Soochow University, Suzhou 215006, People's Republic of China
[47]South China Normal University, Guangzhou 510006, People's Republic of China
[48]Southeast University, Nanjing 211100, People's Republic of China
[49]State Key Laboratory of Particle Detection and Electronics, Beijing 100049, Hefei 230026, People's Republic of China
[50]Sun Yat-Sen University, Guangzhou 510275, People's Republic of China
[51]Suranaree University of Technology, University Avenue 111, Nakhon Ratchasima 30000, Thailand
[52]Tsinghua University, Beijing 100084, People's Republic of China
[53a]Turkish Accelerator Center Particle Factory Group, Istanbul Bilgi University, 34060 Eyup, Istanbul, Turkey
[53b]Near East University, Nicosia, North Cyprus, Mersin 10, Turkey
[54]University of Chinese Academy of Sciences, Beijing 100049, People's Republic of China
[55]University of Groningen, NL-9747 AA Groningen, Netherlands
[56]University of Hawaii, Honolulu, Hawaii 96822, USA
[57]University of Jinan, Jinan 250022, People's Republic of China
[58]University of Manchester, Oxford Road, Manchester M13 9PL, United Kingdom
[59]University of Minnesota, Minneapolis, Minnesota 55455, USA
[60]University of Muenster, Wilhelm-Klemm-Street 9, 48149 Muenster, Germany
[61]University of Oxford, Keble Road, Oxford OX13RH, United Kingdom
[62]University of Science and Technology Liaoning, Anshan 114051, People's Republic of China
[63]University of Science and Technology of China, Hefei 230026, People's Republic of China
[64]University of South China, Hengyang 421001, People's Republic of China
[65]University of the Punjab, Lahore 54590, Pakistan
[66a]University of Turin, I-10125, Turin, Italy
[66b]University of Eastern Piedmont, I-15121, Alessandria, Italy
[66c]INFN, I-10125, Turin, Italy
[67]Uppsala University, Box 516, SE-75120 Uppsala, Sweden
[68]Wuhan University, Wuhan 430072, People's Republic of China
[69]Xinyang Normal University, Xinyang 464000, People's Republic of China
[70]Zhejiang University, Hangzhou 310027, People's Republic of China
[71]Zhengzhou University, Zhengzhou 450001, People's Republic of China

(Received 4 March 2021; accepted 6 July 2021; published 27 August 2021)

The first amplitude analysis of the decay $D_s^+ \to K^- K^+ \pi^+ \pi^0$ is presented using the data samples, corresponding to an integrated luminosity of 6.32 $\mathrm{fb}^{-1}$, collected with the BESIII detector at $e^+e^-$ center-of-mass energies between 4.178 and 4.226 GeV. More than 3000 events selected with a purity of 97.5% are used to perform the amplitude analysis, and nine components are found necessary to describe the data.

[a]Also at Bogazici University, 34342 Istanbul, Turkey.
[b]Also at the Moscow Institute of Physics and Technology, Moscow 141700, Russia.
[c]Also at the Novosibirsk State University, Novosibirsk, 630090, Russia.
[d]Also at the NRC "Kurchatov Institute", PNPI, 188300, Gatchina, Russia.
[e]Also at Istanbul Arel University, 34295 Istanbul, Turkey.
[f]Also at Goethe University Frankfurt, 60323 Frankfurt am Main, Germany.
[g]Also at Key Laboratory for Particle Physics, Astrophysics and Cosmology, Ministry of Education; Shanghai Key Laboratory for Particle Physics and Cosmology; Institute of Nuclear and Particle Physics, Shanghai 200240, People's Republic of China.
[h]Also at Key Laboratory of Nuclear Physics and Ion-beam Application (MOE) and Institute of Modern Physics, Fudan University, Shanghai 200443, People's Republic of China.
[i]Also at Harvard University, Department of Physics, Cambridge, Massachusetts 02138, USA.
[j]Present address: Institute of Physics and Technology, Peace Ave. 54B, Ulaanbaatar 13330, Mongolia.
[k]Also at State Key Laboratory of Nuclear Physics and Technology, Peking University, Beijing 100871, People's Republic of China.
[l]Also at School of Physics and Electronics, Hunan University, Changsha 410082, China.
[m]Also at Guangdong Provincial Key Laboratory of Nuclear Science, Institute of Quantum Matter, South China Normal University, Guangzhou 510006, China.

Relative fractions and phases of the intermediate decays are determined. With the detection efficiency estimated by the results of the amplitude analysis, the branching fraction of $D_s^+ \to K^-K^+\pi^+\pi^0$ decay is measured to be $(5.42 \pm 0.10_{\rm stat} \pm 0.17_{\rm syst})\%$.

DOI: 10.1103/PhysRevD.104.032011

## I. INTRODUCTION

Accurate measurement of $D_s^+$ decays are important for the studies of other decay processes that are dominated by final states involving $D_s^+$ mesons, particularly for those of $B_s^0$ decays [1]. The decay $D_s^+ \to K^-K^+\pi^+\pi^0$ is a Cabibbo-favored decay (the inclusion of charge conjugated reactions is implied throughout this paper). Due to its large branching fraction (BF), it is usually selected as a "tag mode" for the measurement of other decays of the $D_s^+$ meson [2–7]. However, the BF of the $D_s^+ \to K^-K^+\pi^+\pi^0$ decay has a large systematic uncertainty due to the poor knowledge of intermediate-state processes [8,9]. An amplitude analysis of this decay is expected to provide a detailed understanding of its intermediate structures and significantly improve the experimental precision of its decay BF.

The four-body hadronic decays of $D_s^+$ mesons are dominated by two-body intermediate processes, for example $D_s^+ \to AP$ and $D_s^+ \to VV$ decays, where $V$, $A$, and $P$ denote vector, axial-vector, and pseudoscalar mesons, respectively. Measurements of the BFs of these two-body decays are important to test theoretical calculations [10–13] and to better understand the decay mechanisms of the $D_s^+$ meson. In recent years, many measurements of $D_s^+ \to PP$ and $D_s^+ \to VP$ decays have been reported [14]. However, there are few studies focusing on $D_s^+ \to AP$ and $D_s^+ \to VV$ decays. The amplitude analysis of $D_s^+ \to AP$ decay allows the study of substructures involving $K_1(1270)$, $K_1(1400)$, and $f_1(1420)$ mesons. The measurements of the intermediate resonances $K_1(1270)$ and $K_1(1400)$ are also useful for understanding the mixing of these two axial-vector kaons [15]. For $D_s^+ \to VV$, two processes, namely $D_s^+ \to \phi\rho^+$ and $D_s^+ \to \bar{K}^{*0}K^{*+}$, which are represented by the decay diagrams in Fig. 1, can be studied in the $D_s^+ \to K^-K^+\pi^+\pi^0$ decay. The BF of the decay $D_s^+ \to \phi\rho^+$ was measured to be $(8.4^{+1.9}_{-2.3})\%$ [16] by the CLEO experiment based on a data sample corresponding to an integrated luminosity of 689 $\text{pb}^{-1}$ at the $\Upsilon(3S)$ and $\Upsilon(4S)$ resonances and at $e^+e^-$ center-of-mass energies ($E_{\rm cm}$) just below and above the $\Upsilon(4S)$ resonance. The previous most precise determination of the BF of $D_s^+ \to \bar{K}^{*0}K^{*+}$ decay, $(7.2 \pm 2.6)\%$ [17], was performed by the ARGUS experiment using a data sample of 432 $\text{pb}^{-1}$ collected at $E_{\rm cm} = 10.4$ GeV. The goal of the present analysis is to improve the precision of these measurements.

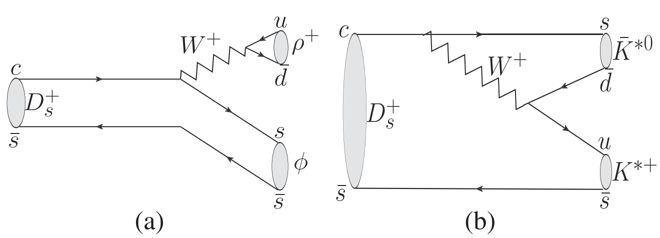


FIG. 1. Decay diagrams of (a) $D_s^+ \to \phi\rho^+$ and (b) $D_s^+ \to \bar{K}^{*0}K^{*+}$ decays.

Moreover, a recent study [18] points out that the measured values of the ratio of $K_1(1270)$ decay ($R_{K_1(1270)} = \frac{\mathcal{B}(K_1(1270)\to K^*\pi)}{\mathcal{B}(K_1(1270)\to K\rho)}$), which are listed in Table I, are inconsistent between different experiments [19–25]. They are expected to be identical under the narrow width approximation for the $K_1(1270)$ meson and assuming $CP$ conservation in strong decays [18]. The decays related to this ratio may be observed in the $D_s^+ \to K^-K^+\pi^+\pi^0$ decay.

In this paper, the first amplitude analysis of the decay $D_s^+ \to K^-K^+\pi^+\pi^0$ is presented using data samples of 6.32 $\text{fb}^{-1}$ collected with the BESIII detector at center-of-mass energies between 4.178 and 4.226 GeV. The amplitude model is constructed with the covariant tensor formalism [26] and described in Sec. IV. The BF measurement is presented in Sec. V.

## II. DETECTOR AND DATASETS

The BESIII detector is a magnetic spectrometer [27,28] located at the Beijing Electron Position Collider (BEPCII) [29]. The cylindrical core of the BESIII detector consists of a helium-based multilayer drift chamber (MDC), a plastic scintillator time-of-flight system (TOF), and a CsI(Tl)

TABLE I. Values of $R_{K_1(1270)}$ determined by different experiments. Fit 1 and fit 2 refer to amplitude analyses performed with the mass and width of the $K_1(1270)^+$ meson fixed or left free in the fit, respectively.

| $R_{K_1(1270)}$ | Process | Experiment |
|---|---|---|
| $0.81 \pm 0.10$ | $D^0 \to K^+K^-\pi^+\pi^-$ | LHCb [19] |
| $1.18 \pm 0.43$ | $D^0 \to K^-K_1^+(1270)$ | CLEO [20] |
| $0.11 \pm 0.06$ | $D^0 \to K^+K_1^-(1270)$ | CLEO [20] |
| $0.19 \pm 0.10$ | $D^0 \to K^-\pi^+\pi^+\pi^-$ | BESIII [21] |
| $0.24 \pm 0.04$ | $D^0 \to K^-\pi^+\pi^+\pi^-$ | LHCb [22] |
| $0.45 \pm 0.05$ | $B^+ \to J/\psi K^+\pi^+\pi^-$ | Belle [23] (Fit 1) |
| $0.30 \pm 0.04$ | $B^+ \to J/\psi K^+\pi^+\pi^-$ | Belle [23] (Fit 2) |
| $0.38 \pm 0.13$ | $K^-p \to K^-\pi^-\pi^+p$ | ACCMOR [24] |
| $0.45 \pm 0.14$ | $D^0 \to K^-K_1^+(1270)$ | CLEO [25] |

TABLE II. The integrated luminosities ($\mathcal{L}_{\rm int}$) and the requirements on $M_{\rm rec}$ for various energies. $M_{\rm rec}$ is defined in Eq. (1).

| $E_{\rm cm}$ (GeV) | $\mathcal{L}_{\rm int}$ (pb$^{-1}$) | $M_{\rm rec}$ (GeV/$c^2$) |
|---|---|---|
| 4.178 | 3189.0 | [2.050, 2.180] |
| 4.189 | 526.7 | [2.048, 2.190] |
| 4.199 | 526.0 | [2.046, 2.200] |
| 4.209 | 517.1 | [2.044, 2.210] |
| 4.219 | 514.6 | [2.042, 2.220] |
| 4.226 | 1047.3 | [2.040, 2.220] |

electromagnetic calorimeter (EMC), which are all enclosed in a superconducting solenoidal magnet providing a 1.0 T magnetic field. The solenoid is supported by an octagonal flux-return yoke with resistive-plate counter muon identifier modules interleaved with steel. The acceptance of charged particles and photons is 93% over the $4\pi$ solid angle. The resolution of charged-particle momentum at 1 GeV/$c$ is 0.5%, while that of the specific ionization energy loss ($dE/dx$) is 6% for electrons from Bhabha scattering. The EMC measures photon energies with a resolution of 2.5% (5%) at 1 GeV in the barrel (end cap) region. The time resolution of the TOF barrel part is 68 ps. The end cap TOF system was upgraded in 2015 with multigap resistive plate chamber technology, providing a time resolution of 60 ps [30,31].

The data samples used in this analysis contain a total integrated luminosity of 6.32 fb$^{-1}$ collected at center-of-mass energies between $E_{\rm cm} = 4.178$ and 4.226 GeV with the BESIII detector. The integrated luminosity of each data sample is shown in Table II. In this energy region, pairs of $D_s^{\pm}D_s^{*\mp}$ mesons are produced. The $D_s^{*\pm}$ meson predominantly decays to $D_s^{\pm}\gamma$ (93.5%), and only a small fraction decays to $D_s\pi^0$ (5.8%) [14]. A double-tag (DT) technique is employed to measure the absolute BF of the $D_s^+$ decays [32]. First, the $D_s^-$ meson is fully reconstructed in one of the following decay modes: $D_s^- \to K_S^0K^-$, $D_s^- \to K^+K^-\pi^-$, $D_s^- \to K_S^0K^-\pi^0$, $D_s^- \to K_S^0K^-\pi^+\pi^-$, $D_s^- \to K_S^0K^+\pi^-\pi^-$, $D_s^- \to \pi^-\eta_{\gamma\gamma}$, $D_s^- \to \pi^-\eta'_{\pi^+\pi^-\eta_{\gamma\gamma}}$, and $D_s^- \to K^-\pi^+\pi^-$. These are referred to as single-tag (ST) events. Second, the $D_s^+ \to K^-K^+\pi^+\pi^0$ decay events are selected.

Generic Monte Carlo (MC) simulated event samples are produced with the GEANT4-based [33,34] software at $E_{\rm cm} = 4.178$–4.226 GeV. The samples include all known open charm decays; the continuum process ($e^+e^- \to q\bar{q}$, $q = u$, $d$, and $s$); Bhabha scattering; the $\mu^+\mu^-$, $\tau^+\tau^-$, and diphoton processes; and the $c\bar{c}$ resonances [$J/\psi$, $\psi(3686)$, and $\psi(3770)$] via initial-state radiation (ISR). The open charm processes are generated using CONEXC [35], and their subsequent decays are modeled by EVTGEN [36] with known BFs from the Particle Data Group (PDG) [14]. The simulation of ISR production of $J/\psi$, $\psi(3686)$, and $\psi(3770)$ mesons is performed with KKMC [37]. The effects of final-state radiation from charged tracks are simulated by PHOTOS [38]. The remaining unknown decays are generated with the LUNDCHARM model [39]. The generic MC sample is used to study backgrounds and determine the efficiencies of tag modes and the signal mode for the BF measurement, in which our amplitude analysis model is used to generate the signal mode events.

A phase-space (PHSP) MC sample is produced with the $D_s^+$ meson decaying to $K^-K^+\pi^+\pi^0$ generated with a uniform distribution and the $D_s^-$ meson decaying to the tag modes. Initially, the PHSP MC sample is used to calculate the normalization integral used in the determination of the amplitude model parameters in the fit to data. Then, the signal MC sample is regenerated with the $D_s^+$ meson decaying to $K^-K^+\pi^+\pi^0$ using the amplitude model and the $D_s^-$ meson decaying to the tag modes. The normalization integral performed with signal MC samples results in more accurate fit parameters of magnitudes and phases and improves the computational efficiency of the MC integration. The signal MC sample is also used to calculate the goodness of the fit in this analysis. The PHSP MC sample is used to determine the efficiency mentioned in Sec. IV A.

## III. EVENT SELECTION

Charged tracks except for those from $K_S^0$ decays are required to have a distance of closest approach to the interaction point (IP) within 1 cm in the transverse plane and within 10 cm along the MDC axis ($z$ axis). The polar angle of the charged track with respect to the $z$ axis $\theta$ is required to satisfy $|\cos\theta| < 0.93$. Kaons and pions are identified by combining the $dE/dx$ information in the MDC and the time-of-flight from the TOF. If the probability of the kaon hypothesis is larger than that of the pion hypothesis, the track is identified as a kaon. Otherwise, the track is identified as a pion. Particle identification (PID) is not performed for the $\pi^+$ or $\pi^-$ from $K_S^0$ decays.

The $\pi^0$ and $\eta$ candidates are reconstructed via diphoton decays. The timing of the electromagnetic showers in the EMC is required to be within [0,700] ns of the trigger time, and the deposited energy must be greater than 25 (50) MeV in the barrel (end cap) region of the EMC. Good showers must satisfy $|\cos\theta| < 0.80$ ($0.86 < |\cos\theta < 0.92$) in the barrel (end cap) and be more than 20° from the nearest charged track. The unconstrained invariant masses of $\pi^0$, $\eta$, and $\eta'$ ($\eta' \to \pi^+\pi^-\eta_{\gamma\gamma}$) are required to be within [115, 150] MeV/$c^2$, [500, 570] MeV/$c^2$, and [946, 970] MeV/$c^2$, respectively. A kinematic fit is performed to constrain $M_{\gamma\gamma}$ to the known $\pi^0$ ($\eta$) mass, and the $\chi^2$ of the corresponding fit is required to be less than 30 (20) for $\pi^0$ ($\eta$) candidates.

The $K_S^0$ candidates are reconstructed in the decay $K_S^0 \to \pi^+\pi^-$. Two oppositely charged tracks with distances of closest approach to the IP less than 20 cm along the $z$ axis are assigned as $\pi^+\pi^-$ without further PID

TABLE III. The $D_s^-$ mass requirements for the eight tag modes.

| Tag mode | Mass window (GeV/$c^2$) |
|---|---|
| $D_s^- \to K_S^0 K^-$ | [1.948, 1.991] |
| $D_s^- \to K^+ K^- \pi^-$ | [1.950, 1.986] |
| $D_s^- \to K_S^0 K^- \pi^0$ | [1.946, 1.987] |
| $D_s^- \to K_S^0 K^- \pi^+ \pi^-$ | [1.958, 1.980] |
| $D_s^- \to K_S^0 K^+ \pi^- \pi^-$ | [1.953, 1.983] |
| $D_s^- \to \pi^- \eta_{\gamma\gamma}$ | [1.930, 2.000] |
| $D_s^- \to \pi^- \eta'_{\pi^+\pi^-\eta_{\gamma\gamma}}$ | [1.940, 1.996] |
| $D_s^- \to K^- \pi^+ \pi^-$ | [1.953, 1.983] |

TABLE IV. Misreconstructed background processes.

| Category | Background | |
|---|---|---|
| (a) | $D_s^+ \to K^+ K^- \pi^+$, | $D_s^- \to \pi^- \pi^0 \eta$ |
| (b) | $D_s^+ \to K^+ K^- \pi^+$, | $D_s^- \to \pi^- \pi^0 \eta'$ |
| (c) | $D_s^+ \to K^+ K^- \pi^+$, | $D_s^- \to K^- \pi^- \pi^+ \pi^0$ |
| (d) | $D^+ \to K^- \pi^+ \pi^+$, | $D^- \to K^+ K^- \pi^- \pi^0$ |
| (e) | $\bar{D}^0 \to K_S^0 K^+ K^-$ | $D^0 \to K^- \pi^+ \pi^0$ |
| (f) | $\bar{D}^0 \to K_S^0 K^+ K^-$, | $D^0 \to K^- \pi^+ \pi^0 \pi^0$ |
| (g) | $D^0 \to K^- \pi^+ \pi^0$, | $\bar{D}^0 \to K^+ \pi^- \pi^+ \pi^-$ |
| (h) | $\bar{D}^0 \to K^+ \pi^- \pi^0$, | $D^0 \to K^- \pi^+ \pi^0$ |

requirements. A constrained vertex fit of each pair of tracks is performed. Candidate $K_S^0$ particles are required to have the $\chi^2$ of the vertex fit less than 100 and an invariant mass of the $\pi^+\pi^-$ pair ($M_{\pi^+\pi^-}$) in the range $[487, 511]$ MeV/$c^2$. In the case of the decay modes $D_s^- \to K_S^0 K^- \pi^0$, $D_s^- \to K_S^0 K^- \pi^+ \pi^-$ and $D_s^- \to K_S^0 K^+ \pi^+ \pi^-$, the decay length of the $K_S^0$ candidates obtained with the secondary vertex fit [40] must be at least two times its fit uncertainty. For the $D_s^- \to K^- \pi^+ \pi^-$ process, $M_{\pi^+\pi^-}$ is required to be outside of the range $[487, 511]$ MeV/$c^2$, to remove possible misidentified events of $D_s^- \to K_S^0 K^-$.

To identify the process $e^+e^- \to D_s^{*-} D_s^+$, the recoil mass $M_{\rm rec}$ of $D_s^-$ candidates is defined as

$$M_{\rm rec} = \sqrt{\left(E_{\rm cm} - \sqrt{|\vec{p}_{D_s^-}|^2 + m_{D_s^-}^2}\right)^2 - |\vec{p}_{D_s^-}|^2}, \quad (1)$$

where $m_{D_s^-}$ is the nominal $D_s^-$ mass [14] and $\vec{p}_{D_s^-}$ is the momentum of the $D_s^-$ candidate. The values of $M_{\rm rec}$ are required to be in the regions depending on the center-of-mass energy as listed in Table II. The $D_s^-$ mass windows for the eight tag modes are shown in Table III.

The $D_s^+$ meson decays with invariant masses $M_{D_s^+}$ in the region $[1.87, 2.06]$ GeV/$c^2$ are selected. Good vertex fits of all charged tracks on both the signal and the tag side are required. A multiconstraint kinematic fit of $e^+e^- \to D_s^{*\pm} D_s^{\mp} \to \gamma D_s^{\pm} D_s^{\mp}$ with $D_s^-$ decaying to one of the tag modes and $D_s^+$ decaying to the signal mode is performed. The set of constraints including four-momentum conservation in the $e^+e^-$ system and the mass constraints of the $\pi^0$ meson, the $D_s^+$ meson, the $D_s^-$ meson, and the $D_s^{*\pm}$ meson is labeled $C_1$. Based on the requirements of $C_1$, a set of constraints $C_2$ is defined by excluding the signal $M_{D_s^+}$ constraint, and $C_3$ is defined by excluding the mass constraints of the $D_s^\pm$ meson on both the signal and tag sides.

If there are multiple candidate combinations in an event, the candidate with the minimum $\chi^2$ of the $C_2$ kinematic fit ($\chi^2_{C_2}$) is chosen. A good $C_1$ kinematic fit is required. To reduce the background while avoiding peaking background, which is caused by constraining the mass of the $D_s^\pm$ meson ($M_{D_s^\pm}$), the $\chi^2$ of the $C_3$ kinematic fit ($\chi^2_{C_3}$) is required to be less than 250.

The classes of background events, which are listed in Table IV, are rejected. For backgrounds categorized as a, b, and c, a $\pi^0$ from the $D_s^-$ decay is wrongly associated to the $D_s^+$ meson on the opposite side. These are vetoed if the $\chi^2$ of the $C_1$ kinematic fit ($\chi^2_{C_1}$) of the reconfigured combination is better than that of the original. For backgrounds categorized as d, the events with $D^+ \to K^-\pi^+\pi^+$ decay versus $D^- \to K^+K^-\pi^-\pi^0$ decay are wrongly reconstructed as $D_s^- \to K^-\pi^+\pi^-$ decay versus $D_s^+ \to K^+K^-\pi^+\pi^0$ decay, when a $\pi^-$ meson from $D^-$ decay is exchanged with a $\pi^+$ meson from $D^+$ decay. If the reconstructed $D^\pm$ masses of the signal and the tag modes fall in the region within 0.055 GeV/$c^2$ of the nominal $M_{D^\pm}$, the events are rejected. For background categories e and f, events with $K_S^0 K^+ K^-$ satisfying $|M_{K_S^0 K^+ K^-} - M_{D^0}^{\rm PDG}| < 0.045$ GeV/$c^2$ are rejected, where $M_{D^0}^{\rm PDG}$ is the nominal mass of $D^0$ [14]. For background category g, the wrong signal combination survives due to exchanging the $\pi^0$ meson from $D^0$ decay and the $\pi^-$ meson from $\bar{D}^0$ decay and misidentifying the $\pi^-$ meson as a $K^-$ meson. They are suppressed by rejecting events satisfying $|M_{K^-\pi^+\pi^0} - M_{D^0}^{\rm PDG}| < 0.055$ GeV/$c^2$ and $|M_{K^+\pi^-\pi^+\pi^-} - M_{D^0}^{\rm PDG}| < 0.055$ GeV/$c^2$. Background type (h) events are suppressed by applying a veto on events with $|M_{K^-\pi^+\pi^0} - M_{D^0}^{\rm PDG}| < 0.045$ GeV/$c^2$.

Events containing a possible misformed $\pi^0$ meson on the signal side are also rejected. Events in which the invariant mass of the higher-energy photon from the signal side combined with a photon from the $D_s^* \to D_s\gamma$ decay is within $[0.12, 0.15]$ GeV/$c^2$ and with $|dM_{\rm recombined}| < |dM|$ are rejected, where $dM$ is the mass difference between the signal $D_s^+$ meson and the tagged $D_s^-$ meson and $dM_{\rm recombined}$ is the corresponding mass difference with the signal $\pi^0$ replaced by the recombined $\pi^0$. A veto is also applied to reject events with recombined mass of the higher-energy photon from the signal side and the photon from the tag side falling within $[0.12, 0.15]$ GeV/$c^2$.

After the full selection, the invariant mass spectra of the signal $D_s^+$ candidates for data samples collected at

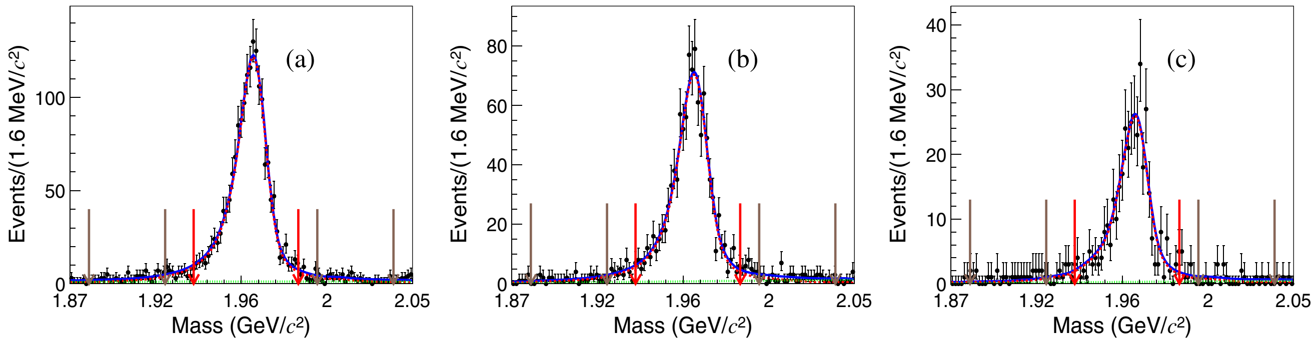


FIG. 2. Fits to the invariant mass spectra of the signal $D_s^+$ candidates for data samples collected at center-of-mass energies (a) 4.178 GeV, (b) 4.189–4.219 GeV, and (c) 4.226 GeV. The black dots with error bars represent data. The red dotted line represents the MC-simulated shape convolved with a Gaussian function. The green dashed lines are the fitted backgrounds. The blue solid line represents the total fitted shape. The red arrows represent the requirements applied in the amplitude analysis, and the brown arrows represent the sideband region.

center-of-mass energies 4.178–4.226 GeV are shown in Fig. 2, together with fits to the mass spectra. There are 1708, 1024, and 356 events retained in the signal region $[1.935, 1.99]$ GeV$/c^2$ for the amplitude analysis with purities, $w_{\rm sig}$, of $97.7 \pm 0.4\%$, $97.3 \pm 0.5\%$, and $97.5 \pm 0.8\%$ at $E_{\rm cm} = 4.178$ GeV, 4.189–4.219 GeV, and 4.226 GeV, respectively. Studies of the generic MC samples show that peaking background is negligible. The background description by the generic MC has been verified by comparisons of data with the generic MC samples in the sideband regions $[1.88, 1.92]$ GeV$/c^2$ and $[2.00, 2.04]$ GeV$/c^2$. A good agreement is found, and the generic MC samples are used to model the residual background contamination in the signal region. The four-momenta of the final-state particles after a two-constraint kinematic fit to the signal candidate, constraining the $D_s^+$ mass and $\pi^0$ mass to their known values [14], are used to perform the amplitude analysis.

## IV. AMPLITUDE ANALYSIS

The amplitude analysis of $D_s^+ \to K^- K^+ \pi^+ \pi^0$ decay is performed by using an unbinned maximum likelihood fit. The likelihood function is constructed with the probability density function (PDF) described in the following, in which the momenta of the four daughter particles are used as inputs.

### A. Likelihood function construction

The PDF used to construct the likelihood of the amplitude is given by

$$f_S(p_j) = \frac{\epsilon(p_j)|M(p_j)|^2 R_4(p_j)}{\int \epsilon(p_j)|M(p_j)|^2 R_4(p_j) dp_j}, \tag{2}$$

where $p_j$ is the set of the final-state particles' four-momenta and $\epsilon(p_j)$ is the detection efficiency parametrized in terms of the final-state particles' four-momenta. The PDF $f_S(p_j)$ is normalized by the integration. The standard element of the four-body PHSP [26] is defined as

$$R_4(p_j)dp_j = \delta^4\left(p_{D_s^+} - \sum_{j=1}^{4} p_j\right) \prod_{j=1}^{4} \frac{d^3 p_j}{(2\pi)^3 2E_j}, \tag{3}$$

where $j$ runs over the four daughter particles and $E_j$ is the energy of particle $j$.

This analysis uses an isobar model formulation, where the signal decay amplitude, $M(p_j)$, is represented as a coherent sum of many two-body amplitude modes

$$M(p_j) = \sum_n c_n A_n(p_j), \tag{4}$$

where $c_n$ is written in the polar form as $\rho_n e^{i\phi_n}$ ($\rho_n$ and $\phi_n$ are the magnitude and phase for the $n$th amplitude, respectively). $A_n(p_j)$ is the $n$th amplitude function modeled as

$$A_n(p_j) = P_n^1(m_1) P_n^2(m_2) S_n(p_j) X_n^1(p_j) X_n^2(p_j) X_n^{D_s^+}(p_j), \tag{5}$$

where the indices 1 and 2 correspond to the two intermediate resonances, respectively. $X_n^{D_s^+}(p_j)$ is the Blatt-Weisskopf barrier factor [26,41–43] for the $D_s^+$ meson, while $P_n^{1,2}(m_1, m_2)$ and $X_n^{1,2}(p_j)$ are the propagators and Blatt-Weisskopf barrier factors of the intermediate resonances 1 and 2, respectively. For nonresonant states, the propagator is set to unity, which can be regarded as a very broad resonance. $S_n(p_j)$ is the spin factor, which is constructed with the covariant tensor formalism [26].

The 2.5% background contribution is described by the background PDF:

$$f_B(p_j) = \frac{B(p_j)R_4(p_j)}{\int B(p_j)R_4(p_j)dp_j}. \tag{6}$$

The background events in the signal region from the generic MC sample are used to model the corresponding background in data. The background shape $B(p_j)$ is derived using a multi-dimensional kernel density estimator [44] with five independent Lorentz invariant variables ($M_{K^-K^+}$, $M_{\pi^+\pi^0}$, $M_{K^-\pi^0}$, $M_{K^-\pi^+}$, and $M_{K^-K^+\pi^0}$) implemented in ROOFIT [45], which models the distribution of an input dataset as a superposition of Gaussian kernels. This background PDF is then added to the signal PDF incoherently, and the combined PDF is written as

$$\begin{aligned} f_T(p_j) &= w_{\text{sig}} f_S(p_j) + (1-w_{\text{sig}}) f_B(p_j) \\ &= w_{\text{sig}} \frac{\epsilon(p_j)|M(p_j)|^2 R_4(p_j)}{\int \epsilon(p_j)|M(p_j)|^2 R_4(p_j)dp_j} \\ &\quad + (1-w_{\text{sig}}) \frac{B(p_j)R_4(p_j)}{\int B(p_j)R_4(p_j)dp_j}, \end{aligned} \tag{7}$$

where the factor $\epsilon(p_j)$ in the numerator can be taken out as in Eq. (8). In this way, the $\epsilon(p_j)$ term, which is independent of the fitted variables, is a constant and can be dropped in the likelihood fit. For the determination of $\epsilon(p_j)$, totally 300 million PHSP MC events at $E_{\text{cm}} = 4.178$ GeV, 4.189–4.219 GeV, and 4.226 GeV are generated, and near 15 million events are selected with the event selection. The background shape is determined from the selected generic MC events; hence, one has to divide the background function by the efficiency, $B_\epsilon \equiv B/\epsilon$. The value $\epsilon(p_j)$ is calculated as the fraction of selected PHSP MC events in the five-dimensional space ($M_{K^-K^+}, M_{\pi^+\pi^0}, M_{K^-\pi^0}$, $M_{K^-\pi^+}, M_{K^-K^+\pi^0}$) with $10\times10\times10\times10\times10$ bins.

The combined PDF becomes

$$\begin{aligned} f_T(p_j) = \epsilon(p_j)R_4(p_j)\Bigg[& w_{\text{sig}} \frac{|M(p_j)|^2}{\int \epsilon(p_j)|M(p_j)|^2 R_4(p_j)dp_j} \\ &+ (1-w_{\text{sig}}) \frac{B_\epsilon(p_j)}{\int \epsilon(p_j)B_\epsilon(p_j)R_4(p_j)dp_j}\Bigg]. \end{aligned} \tag{8}$$

The corresponding likelihood function is defined as

$$L_i = \prod_{k_i=1}^{N^i_{\text{data}}} f_T^{k_i}(p_j), \tag{9}$$

where $i$ denotes the data sample, $k_i$ runs over each event, and $N^i_{\text{data}}$ is the number of events in data sample $i$. The log-likelihood is used to perform the max-likelihood calculation.

The PDFs and the efficiencies are considered separately for three data samples with $E_{\text{cm}} = 4.178$ GeV, 4.189–4.219 GeV, and 4.226 GeV, corresponding to how the data were collected. Therefore, the log-likelihood functions for the three samples are summed up,

$$\ln \mathcal{L} = \sum_{i=1}^{N=3} \ln L_i. \tag{10}$$

The normalization integrals in the denominator of Eq. (8) are obtained by summing over an MC sample

$$\int \epsilon(p_j)|M(p_j)|^2 R_4(p_j)dp_j \approx \frac{1}{N_{\text{MC}}} \sum_{k=1}^{N_{\text{MC}}} \frac{|M(p_j^k)|^2}{|M^{\text{gen}}(p_j^k)|^2}, \tag{11}$$

$$\int \epsilon(p_j)B_\epsilon(p_j)R_4(p_j)dp_j \approx \frac{1}{N_{\text{MC}}} \sum_{k=1}^{N_{\text{MC}}} \frac{B_\epsilon(p_j^k)}{|M^{\text{gen}}(p_j^k)|^2}, \tag{12}$$

where $N_{\text{MC}}$ is the number of the selected MC events and $M^{\text{gen}}(p_j)$ is the amplitude that is set with the parameters used to generate the signal MC sample, which are initially obtained from the results using the PHSP MC integration. $M^{\text{gen}}(p_j)$ is a constant over the whole PHSP. Then, with the results obtained from the fit to data, the signal MC sample is generated and used in MC integration. Totally, 12 million PHSP MC events and 10 million signal MC events are selected at $E_{\text{cm}} = 4.178$ GeV, 4.189–4.219 GeV, and 4.226 GeV with satisfying all selection criteria as that of the data sample.

The effect from the PID, tracking, and reconstruction efficiency differences between data and simulation is considered by multiplying the weight of the MC event by a factor $\gamma_\epsilon$, which is calculated as

$$\gamma_\epsilon(p_j) = \prod_j \frac{\epsilon_{j,\text{data}}(p_j)}{\epsilon_{j,\text{MC}}(p_j)}, \tag{13}$$

where $j = K^\mp$, $K^\pm$, $\pi^\pm$, and $\pi^0$. The signal MC integration becomes

$$\int \epsilon(p_j)|M(p_j)|^2 R_4(p_j)dp_j \approx \frac{1}{N_{\text{MC}}} \sum_{k=1}^{N_{\text{MC}}} \frac{|M(p_j^k)|^2 \gamma_\epsilon(p_j^k)}{|M^{\text{gen}}(p_j^k)|^2}. \tag{14}$$

### 1. Spin factors

For a decay process of the form $a \to bc$, $p_a$, $p_b$, $p_c$ are used to denote the momenta of the particles $a$, $b$, $c$, respectively. The spin projection operator $P^{(S)}_{\mu_1\ldots\mu_S\nu_1\ldots\nu_S}(a)$, for a resonance $a$ with spin $S = 0, 1, 2$ and four-momentum $p_a$, is given by

TABLE V. Spin factor for each decay chain. All operators, i.e., $\tilde{t}$, have the same definitions as Ref. [26]. Scalar, pseudoscalar, vector, and axial-vector states are denoted by $S$, $P$, $V$, and $A$, respectively. $[S]$, $[P]$, and $[D]$ indicate the orbital angular momenta $L = 0$, 1, and 2 of the two-body final states, respectively.

| Decay chain | $S(p)$ |
|---|---|
| $D_s^+[S] \to V_1V_2$ | $\tilde{t}^{(1)\mu}(V_1)\tilde{t}^{(1)}_{\mu}(V_2)$ |
| $D_s^+[P] \to V_1V_2$ | $\epsilon_{\mu\nu\lambda\sigma}p^{\mu}(D_s^+)\tilde{T}^{(1)\nu}(D_s^+)\tilde{t}^{(1)\lambda}(V_1)\tilde{t}^{(1)\sigma}(V_2)$ |
| $D_s^+[D] \to V_1V_2$ | $\tilde{T}^{(2)\mu\nu}(D_s^+)\tilde{t}^{(1)}_{\mu}(V_1)\tilde{t}^{(1)}_{\nu}(V_2)$ |
| $D_s^+ \to AP_1$, $A[S] \to VP_2$ | $\tilde{T}^{(1)\mu}(D_s^+)P^{(1)}_{\mu\nu}(A)\tilde{t}^{(1)\nu}(V)$ |
| $D_s^+ \to AP_1$, $A[D] \to VP_2$ | $\tilde{T}^{(1)\mu}(D_s^+)\tilde{t}^{(2)}_{\mu\nu}(A)\tilde{t}^{(1)\nu}(V)$ |
| $D_s^+ \to AP_1$, $A \to SP_2$ | $\tilde{T}^{(1)\mu}(D_s^+)\tilde{t}^{(1)}_{\mu}(A)$ |
| $D_s^+ \to VS$ | $\tilde{T}^{(1)\mu}(D_s^+)\tilde{t}^{(1)}_{\mu}(V)$ |
| $D_s^+ \to V_1P_1$, $V_1 \to V_2P_2$ | $\epsilon_{\mu\nu\lambda\sigma}p^{\mu}_{V_1}r^{\nu}_{V_1}p^{\lambda}_{P_1}r^{\sigma}_{V_2}$ |
| $D_s^+ \to PP_1$, $P \to VP_2$ | $p^{\mu}(P_2)\tilde{t}^{(1)}_{\mu}(V)$ |
| $D_s^+ \to PP_1$, $P \to SP_2$ | 1 |
| $D_s^+ \to SS$ | 1 |

$$
\begin{aligned}
P^{(0)}(a) &= 1, \\
P^{(1)}_{\mu\mu'}(a) &= -g_{\mu\mu'} + \frac{p_{a,\mu}p_{a,\mu'}}{p_a^2}, \\
P^{(2)}_{\mu\nu\mu'\nu'}(a) &= \frac{1}{2}(P^{(1)}_{\mu\mu'}(a)P^{(1)}_{\nu\nu'}(a) + P^{(1)}_{\mu\nu'}(a)P^{(1)}_{\nu\mu'}(a)) \\
&\quad -\frac{1}{3}P^{(1)}_{\mu\nu}(a)P^{(1)}_{\mu'\nu'}(a), \qquad (15)
\end{aligned}
$$

where $g_{\mu\mu'}$ is the Minkowski metric.

The covariant tensors $\tilde{t}^{(L)}_{\mu_1\ldots\mu_l}(a)$ [26] for the final states of pure orbital angular momentum $L$ are constructed from the relevant momenta $p_a$, $p_b$, $p_c$,

$$
\tilde{t}^{(L)}_{\mu_1\ldots\mu_l}(a) = (-1)^L P^{(L)}_{\mu_1\ldots\mu_L\nu_1\ldots\nu_L}(a)r_a^{\nu_1}\cdots r_a^{\nu_L}, \qquad (16)
$$

where $r_a = p_b - p_c$. The corresponding covariant tensors with $L = 0$, 1, 2 are given as

$$
\begin{aligned}
\tilde{t}^{(0)}(a) &= 1, \\
\tilde{t}^{(1)}_{\mu}(a) &= -P^{(1)}_{\mu\mu'}(a)r_a^{\mu'}, \\
\tilde{t}^{(2)}_{\mu\nu}(a) &= P^{(2)}_{\mu\nu\mu'\nu'}(a)r_a^{\mu'}r_a^{\nu'}. \qquad (17)
\end{aligned}
$$

The 11 types of decay modes used in this analysis are listed in Table V.

### 2. Blatt-Weisskopf barrier factors

The Blatt-Weisskopf barrier $X(p_j)$ [26,41–43] is a barrier function for a two-body decay process, $a \to bc$. The Blatt-Weisskopf barrier depends on the angular momenta and the momenta of the final-state particles in the rest frame of the parent particle. The definition is given by

$$
\begin{aligned}
X_{L=0}(q) &= 1, \\
X_{L=1}(q) &= \sqrt{\frac{2}{q^2 + (1/R)^2}}, \\
X_{L=2}(q) &= \sqrt{\frac{13}{q^4 + 3q^2(1/R)^2 + 9(1/R)^4}}, \qquad (18)
\end{aligned}
$$

where $L$ denotes the orbital angular momentum; $R$ is the effective radius of the barrier; the values of $R$ used in this analysis are taken to be 3.0 and 5.0 $\mathrm{GeV}^{-1}$ for intermediate resonances and the $D_s^+$ meson, respectively [46]; and $q$ is the magnitude of the momenta of the final-state particles in the rest system of the parent particle.

For a process $a \to bc$, $s_i = E_i^2 - p_i^2$ is defined, where $i$ denotes $a$, $b$, $c$ and $E_i$, $p_i$ are the particle's energy and momentum, such that

$$
q^2 = \frac{(s_a + s_b - s_c)^2}{4s_a} - s_b. \qquad (19)
$$

### 3. Propagators

The relativistic Breit-Wigner (RBW) function is used as the propagator for the resonances $\phi$, $\bar{K}^{*0}$, $K^{*\pm}$, $\bar{K}_1^0(1270)$, $\bar{K}_1^0(1400)$, $f_1(1510)$, $f_1(1420)$, and $\eta(1475)$, and their masses and widths are fixed to their PDG values [14], as listed in Table VI.

The RBW function is given by

$$
P(m) = \frac{1}{(m_0^2 - m^2) - im_0\Gamma(m)}, \qquad (20)
$$

where $m = \sqrt{E^2 - p^2}$ and $m_0$ is the nominal mass of the resonance and $\Gamma(m)$ is given by

$$
\Gamma(m) = \Gamma_0\left(\frac{q}{q_0}\right)^{2L+1}\left(\frac{m_0}{m}\right)\left(\frac{X_L(q)}{X_L(q_0)}\right)^2, \qquad (21)
$$

where $q_0$ indicates the value of $q$ when $s_a = m_0^2$.

Considering the obvious mass deviation, the mass and width of $\bar{K}_1^0(1270)$ are set to the average values (shown in Table VI) without including the results from Belle [47].

The $\rho^+$ meson is parametrized with the Gounaris-Sakurai line shape (GS) [48], which is given by

TABLE VI. The masses and widths of intermediate resonances used in this analysis.

| Resonance | Mass ($\mathrm{MeV}/c^2$) | Width (MeV) |
|---|---|---|
| $\phi$ | $1019.461 \pm 0.016$ | $4.249 \pm 0.013$ |
| $\rho^+$ | $775.11 \pm 0.34$ | $149.1 \pm 0.8$ |
| $\bar{K}^{*0}$ | $895.55 \pm 0.20$ | $47.3 \pm 0.5$ |
| $K^{*\pm}$ | $891.66 \pm 0.26$ | $50.8 \pm 0.9$ |
| $\bar{K}_1^0(1270)$ | $1272 \pm 7$ | $87 \pm 7$ |
| $\bar{K}_1^0(1400)$ | $1403 \pm 7$ | $174 \pm 13$ |
| $f_1(1420)$ | $1426.3 \pm 0.9$ | $54.5 \pm 2.6$ |
| $\eta(1475)$ | $1475 \pm 4$ | $90 \pm 9$ |
| $a_0^0(980)$ | $990 \pm 1$ | $g_{\eta\pi(K\bar{K})}$ (see text) |

$$P_{\mathrm{GS}}(m) = \frac{1 + d\frac{\Gamma_0}{m_0}}{(m_0^2 - m^2) + f(m) - i m_0 \Gamma(m)}. \tag{22}$$

The function $f(m)$ is given by

$$f(m) = \Gamma_0 \frac{m_0^2}{q_0^3} \times \left[ q^2 (h(m) - h(m_0)) + (m_0^2 - m^2) q_0^2 \frac{dh}{d(m^2)}\Big|_{m_0^2} \right], \tag{23}$$

where

$$h(m) = \frac{2q}{\pi m} \ln\left(\frac{m + 2q}{2m_\pi}\right), \tag{24}$$

$$\frac{dh}{d(m^2)}\Big|_{m_0^2} = h(m_0)[(8q_0^2)^{-1} - (2m_0^2)^{-1}] + (2\pi m_0^2)^{-1} \tag{25}$$

and $m_\pi$ is the charged pion mass.

The normalization condition at $P_{\mathrm{GS}}(0)$ fixes the parameter $d = f(0)/(\Gamma_0 m_0)$. It is found to be

$$d = \frac{3m_\pi^2}{\pi q_0^2} \ln\left(\frac{m_0 + 2q_0}{2m_\pi}\right) + \frac{m_0}{2\pi q_0} - \frac{m_\pi^2 m_0}{\pi q_0^3}. \tag{26}$$

The $a_0(980)$ meson line shape is parametrized by the Flatté formula [49],

$$P_{a_0(980)} = \frac{1}{(m_0^2 - s_a) - i(g_{\eta\pi}^2 \rho_{\eta\pi} + g_{K\bar{K}}^2 \rho_{K\bar{K}})}, \tag{27}$$

where $m_0$ is the mass of $a_0(980)$ and $g_{\eta\pi(K\bar{K})}^2$ is the coupling constant. These parameters are fixed at the values given in Ref. [50], in which $m_0 = (0.990 \pm 0.001)\ \mathrm{GeV}/c^2$, $g_{\eta\pi}^2 = (0.341 \pm 0.004)\ \mathrm{GeV}^2/c^4$, and $g_{K\bar{K}}^2 = (0.892 \pm 0.022) g_{\eta\pi}^2$. The $\rho_{\eta\pi(K\bar{K})}$ is the PHSP factor and is given by $\rho_{\eta\pi(K\bar{K})} = 2q/\sqrt{s_a}$.

TABLE VII. The $K\pi$ S-wave parameters, obtained from a fit to the $D^0 \to K_S^0 \pi^+ \pi^-$ Dalitz plot from the *BABAR* and Belle experiments [51]. The first uncertainties are statistical, and the second are systematic.

| | |
|---|---|
| $M(\mathrm{GeV}/c^2)$ | $1.441 \pm 0.002$ |
| $\Gamma(\mathrm{GeV})$ | $0.193 \pm 0.004$ |
| $F$ | $0.96 \pm 0.07$ |
| $\phi_F(\mathrm{deg})$ | $0.1 \pm 0.3$ |
| $R$ | 1 (fixed) |
| $\phi_R(\mathrm{deg})$ | $-109.7 \pm 2.6$ |
| $a$ | $0.113 \pm 0.006$ |
| $r$ | $-33.8 \pm 1.8$ |

The $K\pi$ S wave is modeled by a parametrization from scattering data [51], which is built from a Breit-Wigner shape for the $K_0^*(1430)$ resonance combined with an effective range parametrization for the nonresonant component with a phase shift given by

$$A(m) = F \sin\delta_F e^{i\delta_F} + R \sin\delta_R e^{i\delta_R} e^{i2\delta_F}, \tag{28}$$

with

$$\delta_F = \phi_F + \cot^{-1}\left[\frac{1}{aq} + \frac{rq}{2}\right],$$
$$\delta_R = \phi_R + \tan^{-1}\left[\frac{M\Gamma(m_{K\pi})}{M^2 - m_{K\pi}^2}\right],$$

where $a$ and $r$ are the scattering length and effective interaction length, respectively. The parameters $F(\phi_F)$ and $R(\phi_R)$ are the magnitude (phase) for the nonresonant state and resonance terms, respectively. The parameters $M$, $F$, $\phi_F$, $R$, $\phi_R$, $a$, and $r$ are fixed to the results of the $D^0 \to K_S^0 \pi^+ \pi^-$ analysis by the *BABAR* and Belle experiments [51] and are given in Table VII.

### B. Fit fractions and statistical uncertainty

The fit fractions of the individual components (amplitudes) are calculated according to the fit results. In the calculation, a large PHSP MC sample (12 million events) with neither detector acceptance nor resolution included is used. The fit fraction (FF) for a component or an amplitude is defined as

$$\mathrm{FF}_n = \frac{\int |c_n A_n(p_j)|^2 R_4(p_j) dp_j}{\int |M(p_j)|^2 R_4(p_j) dp_j} \approx \frac{\sum_{k=1}^{N_{\mathrm{g,ph}}} |\tilde{A}_n(p_j^k)|^2}{\sum_{k=1}^{N_{\mathrm{g,ph}}} |M(p_j^k)|^2}, \tag{29}$$

where the integration is approximated by the PHSP MC summation at the generator level, $\tilde{A}_n(p_j^k)$ is either the $n$th amplitude ($\tilde{A}_n(p_j^k) = c_n A_n(p_j^k)$) or the $n$th component of a coherent sum of amplitudes ($\tilde{A}_n(p_j^k) = \sum c_{n_i} A_{n_i}(p_j^k)$), and $N_{\mathrm{g,ph}}$ is the number of PHSP MC events.

TABLE VIII. The nine components in the nominal amplitude model.

| |
|---|
| $D_s^+ \to \phi\rho^+$ |
| $D_s^+ \to \bar{K}^{*0}K^{*+}$ |
| $D_s^+ \to a_0^0(980)\rho^+$ |
| $D_s^+ \to \bar{K}_1^0(1270)K^+(\bar{K}_1^0(1270) \to K^-\rho^+)$ |
| $D_s^+ \to \bar{K}_1^0(1270)K^+(\bar{K}_1^0(1270) \to K^*\pi)$ |
| $D_s^+ \to \bar{K}_1^0(1400)K^+(\bar{K}_1^0(1400) \to K^*\pi)$ |
| $D_s^+ \to f_1(1420)\pi^+(f_1(1420) \to K^{*\mp}K^\pm)$ |
| $D_s^+ \to f_1(1420)\pi^+(f_1(1420) \to a_0^0(980)\pi^0)$ |
| $D_s^+ \to \eta(1475)\pi^+(\eta(1475) \to a_0^0(980)\pi^0)$ |

For the statistical uncertainty of FF, it is impractical to analytically propagate the uncertainties of the FFs from those of the magnitudes and phases. Instead, the variables are randomly perturbed within their uncertainties obtained from the fit, and the FFs are calculated to determine the statistical uncertainties. The distribution of each FF is fitted with a Gaussian function, and the width is the statistical uncertainty of the FF.

### C. Results of the amplitude analysis

The amplitude of the $D_s^+[S] \to \phi\rho^+$ decay is expected to have the largest FF. Thus, this amplitude is chosen as the reference (its phase is fixed to 0, and the magnitude is fixed to 1). The notation $[S]$ denotes a relative orbital angular momentum $L = 0$ between daughters in a decay, and similarly for $[P]$ ($L = 1$), $[D]$ ($L = 2$). In addition, some necessary physical relations are fixed, as shown in the Appendix A.

The fit to the data is initially performed with a baseline model including the amplitudes of $D_s^+ \to \phi\rho^+$, $D_s^+ \to \bar{K}^{*0}K^{*+}$, $D_s^+ \to \bar{K}_1^0(1270)K^+$ $[\bar{K}_1^0(1270) \to K^-\rho^+$ and $K^*\pi]$, and $D_s^+ \to \bar{K}_1^0(1400)K^+$ $[\bar{K}_1^0(1400) \to K^*\pi]$ decays, as the $\phi$, $\rho^+$, $\bar{K}^{*0}$, $K^{*+}$, $K^{*-}$, $\bar{K}_1^0(1270)$, and $\bar{K}_1^0(1400)$ resonances are clearly observed in the corresponding invariant mass spectra. The statistical significances (SSs) of the above amplitudes, which are determined from the changes in log-likelihood and the numbers of degrees of freedom (NDOF) when the fits are performed with and without the amplitude included, are all much larger than $4\sigma$.

Starting from the baseline model above, the amplitudes involving $f_1(1420)$, $f_1(1510)$, $\eta(1405)$, and $\eta(1475)$ resonances are added to improve the fit quality of the $K^-K^+\pi^0$ invariant mass spectrum. The amplitudes with significances larger than $4\sigma$ are retained for the next iteration. The amplitudes of $D_s^+ \to f_1(1420)\pi^+$ ($f_1(1420) \to K^*K$) and $D_s^+ \to \eta(1475)\pi^+$ $[\eta(1475) \to a_0^0(980)\pi^0]$ decays have significances larger than $5\sigma$, and the amplitude of $D_s^+ \to f_1(1420)\pi^+$ $[f_1(1420) \to a_0^0(980)\pi^0]$ decay improves the fit of the $K^-K^+\pi^0$ mass spectrum. Then, other amplitudes are tested, but only the $D_s^+ \to a_0^0(980)\rho^+$ decay is significant ($9\sigma$). Finally, 18 amplitudes are retained in the nominal fit, which are categorized into nine processes, as shown in Table VIII. The amplitudes of the nominal fit are listed in Table IX. Other possible processes with significance less than $3\sigma$ are listed in Appendix B

The fit results with phases, FFs and SSs for each amplitude are shown in Table IX. The ratio $\frac{\mathcal{B}(D_s^+\to\bar{K}_1^0(1270)K^+,\bar{K}_1^0(1270)\to K^{*-}\pi^+)}{\mathcal{B}(D_s^+\to\bar{K}_1^0(1270)K^+,\bar{K}_1^0(1270)\to K^-\rho^+)}$ is determined to be $0.33 \pm 0.05_{\rm stat} \pm 0.06_{\rm syst}$ in this analysis, accounting for correlations. The fit projections of three data samples on the invariant masses are shown in Fig. 3.

### D. Goodness of fit

The goodness of the fit is checked with five invariant masses, $M_{K^-\pi^+}$, $M_{\pi^+\pi^0}$, $M_{K^-K^+}$, $M_{K^-\pi^+\pi^0}$, and $M_{K^-K^+\pi^0}$, which are divided into cells of equal size. When cells contain fewer than 10 events, adjacent cells are combined until the number of events in each cell is larger than 10. For each cell, $\chi_p = \frac{N_p - N_p^{\rm exp}}{\sqrt{N_p^{\rm exp}}}$ is calculated, and the goodness of the fit is given by $\chi^2 = \sum_{p=1}^n \chi_p^2$, where $N_p$ and $N_p^{\rm exp}$ are the number of the observed events and the number determined by the fit results in the $p$th cell, respectively, and $n$ is the total number of cells. NDOF is given by $(n-1) - n_{\rm par}$, where $n_{\rm par}$ is the number of the free parameters in the fit. Overall, the value of $\chi^2$/NDOF is determined to be 316.8/273.

### E. Systematic uncertainties

Systematic uncertainties from the amplitude model, the background, and the fit bias are considered. The systematic uncertainties of phases ($\phi$) and FFs for different amplitudes are shown in Tables X and XI, respectively.

(i) *Amplitude model*

The systematic uncertainties related to the amplitude model involve the masses and widths of the intermediate resonances, the line shape of the $\rho^+$ meson, the parameters of $a_0(980)$ resonance, and the barrier effective radii of the $D_s^+$ meson and other intermediate states.

(1) The uncertainties associated with the masses and widths of the intermediate resonances [$\phi$, $\rho^+$, $\bar{K}^{*0}$, $K^{*\pm}$, $\bar{K}_1^0(1270)$, $\bar{K}_1^0(1400)$, $f_1(1420)$, and $\eta(1475)$] are estimated by varying the corresponding masses and widths listed in Table VI within $1\sigma$.

(2) For the line shape of the $\rho^+$ meson, an alternative line shape parametrization with RBW replacing GS is used.

(3) The coupling constants and mass of $a_0(980)$ resonance are varied within the uncertainties given by Ref. [50].

(4) The barrier effective radii ($R$) of the $D_s^+$ meson and other intermediate states are assumed to have a

TABLE IX. Phase, FF, and SS for the different amplitudes, labeled as I, II..., XIV. Groups of related amplitudes are separated by horizontal lines. The last row of each group gives the total fit fraction of the above components with interferences considered. The amplitudes VIII, IX, X, and XII are constructed by two subamplitudes with fixed relations (see Appendix A). The $\rho^+$ resonance decays to $\pi^+\pi^0$. The $\phi$ and $a_0^0(980)$ resonances decay to $K^-K^+$. The $\bar{K}^{*0}$ resonance decays to $K^-\pi^+$, and the $K^{*\pm}$ resonance decays to $K^\pm\pi^0$. $K^*\pi$ indicates $\bar{K}^{*0}\pi^0$ and $K^{*-}\pi^+$. The first and second uncertainties are statistical and systematic, respectively.

| Label | Amplitude | Phase ($\phi_n$) | FF (%) | SS ($\sigma$) |
|---|---|---|---|---|
| I | $D_s^+[S] \to \phi\rho^+$ | 0.0 (fixed) | $38.68 \pm 1.42 \pm 2.17$ | >20 |
| II | $D_s^+[P] \to \phi\rho^+$ | $-1.46 \pm 0.05 \pm 0.02$ | $9.64 \pm 0.84 \pm 0.30$ | 17.1 |
| III | $D_s^+[D] \to \phi\rho^+$ | $1.46 \pm 0.07 \pm 0.04$ | $3.36 \pm 0.75 \pm 0.27$ | 4.5 |
| | $D_s^+ \to \phi\rho^+$ | ... | $50.81 \pm 1.01 \pm 2.20$ | ... |
| IV | $D_s^+[S] \to \bar{K}^{*0}K^{*+}$ | $-2.15 \pm 0.06 \pm 0.05$ | $16.32 \pm 0.95 \pm 0.33$ | >20 |
| V | $D_s^+[P] \to \bar{K}^{*0}K^{*+}$ | $-0.52 \pm 0.07 \pm 0.04$ | $6.87 \pm 0.55 \pm 0.26$ | 16.1 |
| VI | $D_s^+[D] \to \bar{K}^{*0}K^{*+}$ | $-1.57 \pm 0.08 \pm 0.03$ | $3.34 \pm 0.55 \pm 0.18$ | 12.1 |
| | $D_s^+ \to \bar{K}^{*0}K^{*+}$ | ... | $23.15 \pm 0.89 \pm 0.74$ | ... |
| VII | $D_s^+ \to \bar{K}_1^0(1270)K^+$, $\bar{K}_1^0(1270) \to K^-\rho^+$ | $1.87 \pm 0.08 \pm 0.17$ | $10.44 \pm 0.81 \pm 0.73$ | >20 |
| | $D_s^+ \to \bar{K}_1^0(1270)K^+$, $\bar{K}_1^0(1270)[S] \to \bar{K}^{*0}\pi^0$ | ... | $1.40 \pm 0.26 \pm 0.17$ | ... |
| | $D_s^+ \to \bar{K}_1^0(1270)K^+$, $\bar{K}_1^0(1270)[S] \to K^{*-}\pi^+$ | ... | $2.60 \pm 0.48 \pm 0.31$ | ... |
| VIII | $D_s^+ \to \bar{K}_1^0(1270)K^+$, $\bar{K}_1^0(1270)[S] \to K^*\pi$ | $-0.25 \pm 0.11 \pm 0.12$ | $3.88 \pm 0.71 \pm 0.45$ | 10.8 |
| | $D_s^+ \to \bar{K}_1^0(1270)K^+$, $\bar{K}_1^0(1270)[D] \to \bar{K}^{*0}\pi^0$ | ... | $0.45 \pm 0.11 \pm 0.10$ | ... |
| | $D_s^+ \to \bar{K}_1^0(1270)K^+$, $\bar{K}_1^0(1270)[D] \to K^{*-}\pi^+$ | ... | $0.86 \pm 0.20 \pm 0.17$ | ... |
| IX | $D_s^+ \to \bar{K}_1^0(1270)K^+$, $\bar{K}_1^0(1270)[D] \to K^*\pi$ | $1.52 \pm 0.11 \pm 0.15$ | $1.34 \pm 0.31 \pm 0.27$ | 8.3 |
| | $D_s^+ \to \bar{K}_1^0(1270)K^+$, $\bar{K}_1^0(1270) \to K^*\pi$ | ... | $5.43 \pm 0.69 \pm 0.76$ | ... |
| | $D_s^+ \to \bar{K}_1^0(1400)K^+$, $\bar{K}_1^0(1400)[S] \to \bar{K}^{*0}\pi^0$ | ... | $2.90 \pm 0.39 \pm 0.44$ | ... |
| | $D_s^+ \to \bar{K}_1^0(1400)K^+$, $\bar{K}_1^0(1400)[S] \to K^{*-}\pi^+$ | ... | $5.37 \pm 0.73 \pm 0.82$ | ... |
| X | $D_s^+ \to \bar{K}_1^0(1400)K^+$, $\bar{K}_1^0(1400)[S] \to K^*\pi$ | $-0.92 \pm 0.07 \pm 0.05$ | $8.03 \pm 1.09 \pm 1.22$ | 13.1 |
| XI | $D_s^+ \to a_0^0(980)\rho^+$ | $2.15 \pm 0.08 \pm 0.08$ | $3.46 \pm 0.58 \pm 0.61$ | 9.9 |
| | $D_s^+ \to f_1(1420)\pi^+$, $f_1(1420) \to K^{*-}K^+$ | ... | $1.56 \pm 0.28 \pm 0.17$ | ... |
| | $D_s^+ \to f_1(1420)\pi^+$, $f_1(1420) \to K^{*+}K^-$ | ... | $1.56 \pm 0.28 \pm 0.17$ | ... |
| XII | $D_s^+ \to f_1(1420)\pi^+$, $f_1(1420) \to K^{*\mp}K^\pm$ | $2.13 \pm 0.08 \pm 0.05$ | $2.39 \pm 0.43 \pm 0.25$ | 9.5 |
| XIII | $D_s^+ \to f_1(1420)\pi^+$, $f_1(1420) \to a_0^0(980)\pi^0$ | $2.95 \pm 0.13 \pm 0.06$ | $0.77 \pm 0.27 \pm 0.09$ | 4.5 |
| XIV | $D_s^+ \to \eta(1475)\pi^+$, $\eta(1475) \to a_0^0(980)\pi^0$ | $0.61 \pm 0.10 \pm 0.06$ | $1.37 \pm 0.32 \pm 0.34$ | 8.0 |

uniform distribution. For the $D_s^+$ meson, the value of $R$ is varied between 4.0 and 6.0 GeV$^{-1}$. For the intermediate states, $R$ is varied between 2.0 and 4.0 GeV$^{-1}$.

(ii) *Experimental effects*

Experimental effects are related to the PID, tracking, and reconstruction efficiency differences between data and MC and are reflected in the factor $\gamma_\epsilon$ in Eq. (13). The PID efficiencies are studied using clean samples of $e^+e^- \to K^+K^-K^+K^-$, $K^+K^-\pi^+\pi^-$, $K^+K^-\pi^+\pi^-\pi^0$, $\pi^+\pi^-\pi^+\pi^-$, and $\pi^+\pi^-\pi^+\pi^-\pi^0$ decays, while two clean samples of the continuum process $K^+K^-\pi^+\pi^-$ and the $e^+e^- \to K^+K^-\pi^+\pi^-\pi^0$ decay are used for the studies of the tracking efficiencies and the $\pi^0$ reconstruction efficiency, respectively. These efficiencies are also used in the BF measurement (Sec. V C). The PID and tracking systematic uncertainties are taken as the efficiency differences between data and MC simulation. The uncertainties associated with $\gamma_\epsilon$ are obtained by performing alternative amplitude analyses varying PID and tracking efficiencies according to their uncertainties.

(iii) *Background*

The MC background yields are varied within their uncertainties, and the largest difference from the fits is taken as the uncertainty from the background level. The background shape $B(p_j)$ mentioned in Eq. (6), derived from another combination of five variables ($M_{K^-K^+}, M_{\pi^+\pi^0}, M_{K^+\pi^0}, M_{K^-\pi^+}$, and $M_{K^-K^+\pi^0}$) is considered and applied. The square root of the quadratic sum of these two uncertainties is taken as the background uncertainty.

(iv) *Fit bias*

The uncertainty due to the fit procedure is evaluated by studying signal MC samples. An ensemble of 300 signal MC samples is generated

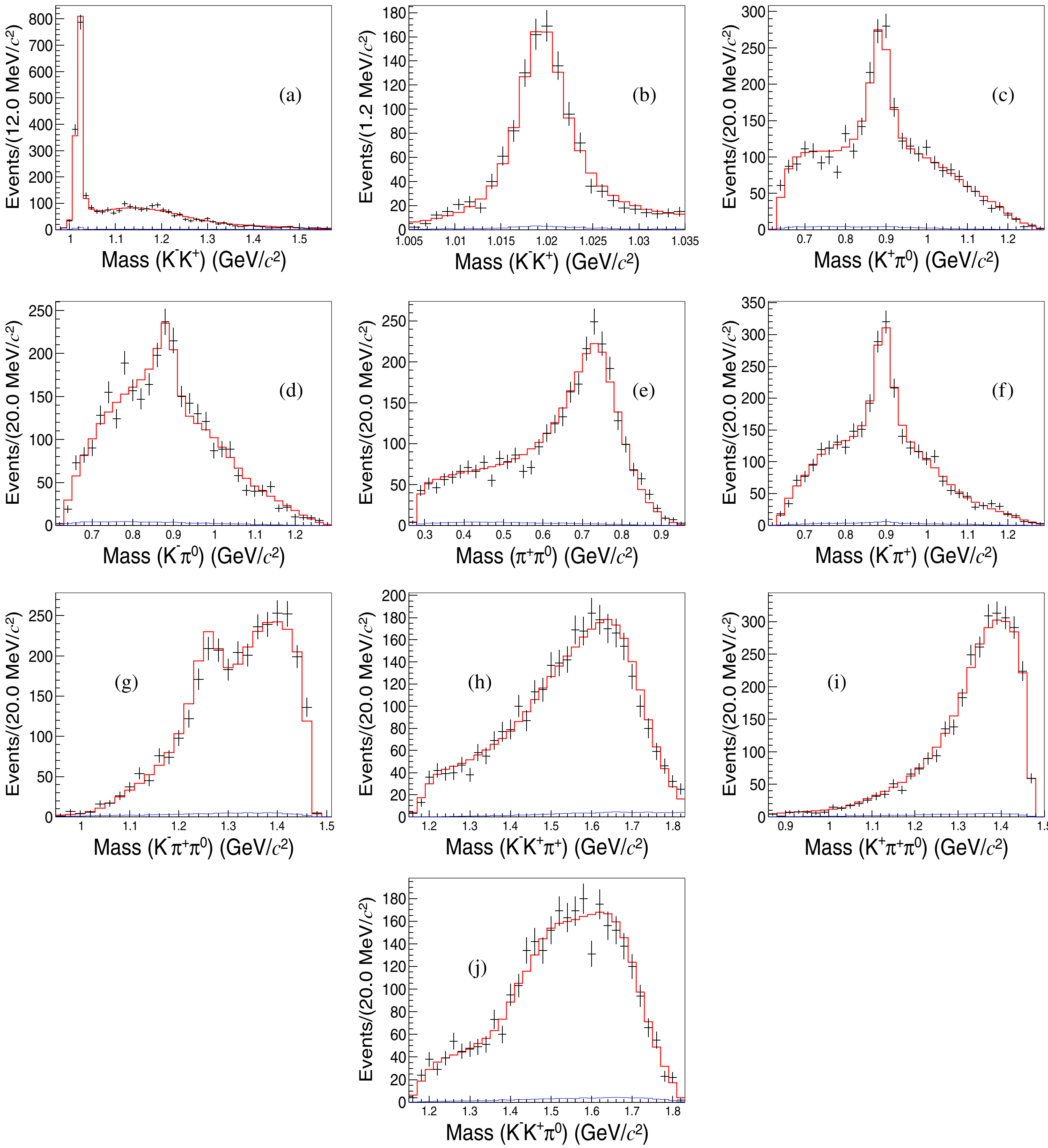


FIG. 3. Invariant mass distributions of (a) $K^-K^+$, (c) $K^+\pi^0$, (d) $K^-\pi^0$, (e) $\pi^+\pi^0$, (f) $K^-\pi^+$, (g) $K^-\pi^+\pi^0$, (h) $K^-K^+\pi^+$, (i) $K^+\pi^+\pi^0$, and (j) $K^-K^+\pi^0$, where the black points with error bars are data, and the red histograms are for the fit projections. The blue histograms are the backgrounds. Plot (b) shows the $\phi$ mass region of plot (a) with an expanded scale.

according to the nominal result in this analysis. After applying the selection criteria, each of these samples has the same size as the data sample and is used to perform the same amplitude analysis. The pull of each parameter is defined as $\frac{\mathrm{Out}(i)-\mathrm{In}(i)}{\sigma_{\mathrm{stat.}}(i)}$, where $i$ denotes different parameters, $\mathrm{In}(i)$ denotes the input value as taken from the nominal fit to data, $\mathrm{Out}(i)$ is the value obtained from the fit to a signal MC sample, and $\sigma_{\mathrm{stat.}}(i)$ is

TABLE X. The phase systematic uncertainty sources (in units of statistical standard deviations) are 1) mass and width, 2) shape of the $\rho^+$ meson, 3) parameters of the $a_0^0(980)$ meson, 4) $R$ value, 5) experimental effects, 6) background, and 7) fit bias.

| Phase ($\phi$) | 1 | 2 | 3 | 4 | 5 | 6 | 7 | Total |
|---|---|---|---|---|---|---|---|---|
| $D_s^+[S] \to \phi\rho^+$ | 0 (fixed) | | | | | | | |
| $D_s^+[P] \to \phi\rho^+$ | 0.11 | 0.05 | 0.00 | 0.39 | 0.00 | 0.02 | 0.06 | 0.41 |
| $D_s^+[D] \to \phi\rho^+$ | 0.10 | 0.23 | 0.03 | 0.56 | 0.06 | 0.06 | 0.06 | 0.62 |
| $D_s^+[S] \to \bar{K}^{*0}K^{*+}$ | 0.74 | 0.10 | 0.09 | 0.26 | 0.08 | 0.18 | 0.06 | 0.82 |
| $D_s^+[P] \to \bar{K}^{*0}K^{*+}$ | 0.49 | 0.05 | 0.05 | 0.20 | 0.04 | 0.08 | 0.06 | 0.55 |
| $D_s^+[D] \to \bar{K}^{*0}K^{*+}$ | 0.34 | 0.01 | 0.01 | 0.11 | 0.00 | 0.03 | 0.06 | 0.37 |
| $D_s^+ \to \bar{K}_1^0(1270)K^+,\ \bar{K}_1^0(1270) \to K^-\rho^+$ | 1.95 | 0.05 | 0.13 | 0.63 | 0.13 | 0.24 | 0.06 | 2.07 |
| $D_s^+ \to \bar{K}_1^0(1270)K^+,\ \bar{K}_1^0(1270)[S] \to K^*\pi$ | 0.92 | 0.17 | 0.17 | 0.47 | 0.18 | 0.23 | 0.06 | 1.10 |
| $D_s^+ \to \bar{K}_1^0(1270)K^+,\ \bar{K}_1^0(1270)[D] \to K^*\pi$ | 1.24 | 0.18 | 0.18 | 0.32 | 0.20 | 0.29 | 0.06 | 1.36 |
| $D_s^+ \to \bar{K}_1^0(1400)K^+,\ \bar{K}_1^0(1400)[S] \to K^*\pi$ | 0.74 | 0.01 | 0.00 | 0.14 | 0.00 | 0.01 | 0.06 | 0.76 |
| $D_s^+ \to a_0^0(980)\rho^+$ | 0.69 | 0.14 | 0.02 | 0.77 | 0.05 | 0.05 | 0.06 | 1.05 |
| $D_s^+ \to f_1(1420)\pi^+,\ f_1(1420) \to K^{*\mp}K^\pm$ | 0.42 | 0.10 | 0.10 | 0.46 | 0.15 | 0.09 | 0.07 | 0.67 |
| $D_s^+ \to f_1(1420)\pi^+,\ f_1(1420) \to a_0^0(980)\pi^0$ | 0.30 | 0.03 | 0.12 | 0.31 | 0.02 | 0.11 | 0.05 | 0.47 |
| $D_s^+ \to \eta(1475)\pi^+,\ \eta(1475) \to a_0^0(980)\pi^0$ | 0.43 | 0.08 | 0.06 | 0.45 | 0.05 | 0.01 | 0.08 | 0.63 |

TABLE XI. The FF systematic uncertainty sources (in units of statistical standard deviations) are 1) mass and width, 2) shape of $\rho^+$ meson, 3) parameters of $a_0^0(980)$ meson, 4) $R$ value, 5) experimental effects, 6) background, and 7) fit bias. The last row is the systematic uncertainty of the ratio $\frac{\mathcal{B}(D_s^+\to\bar{K}_1^0(1270)K^+,\bar{K}_1^0(1270)\to K^{*-}\pi^+)}{\mathcal{B}(D_s^+\to\bar{K}_1^0(1270)K^+,\bar{K}_1^0(1270)\to K^-\rho^+)}$.

| FF | 1 | 2 | 3 | 4 | 5 | 6 | 7 | Total |
|---|---|---|---|---|---|---|---|---|
| $D_s^+[S] \to \phi\rho^+$ | 1.09 | 0.33 | 0.33 | 0.54 | 0.58 | 0.55 | 0.07 | 1.53 |
| $D_s^+[P] \to \phi\rho^+$ | 0.28 | 0.08 | 0.08 | 0.14 | 0.04 | 0.11 | 0.07 | 0.36 |
| $D_s^+[D] \to \phi\rho^+$ | 0.26 | 0.08 | 0.09 | 0.12 | 0.08 | 0.09 | 0.13 | 0.36 |
| $D_s^+ \to \phi\rho^+$ | 1.46 | 0.33 | 0.45 | 1.00 | 0.88 | 0.72 | 0.07 | 2.18 |
| $D_s^+[S] \to \bar{K}^{*0}K^{*+}$ | 0.19 | 0.03 | 0.07 | 0.12 | 0.23 | 0.09 | 0.06 | 0.35 |
| $D_s^+[P] \to \bar{K}^{*0}K^{*+}$ | 0.34 | 0.04 | 0.09 | 0.22 | 0.20 | 0.14 | 0.07 | 0.48 |
| $D_s^+[D] \to \bar{K}^{*0}K^{*+}$ | 0.13 | 0.01 | 0.03 | 0.23 | 0.11 | 0.04 | 0.13 | 0.32 |
| $D_s^+ \to \bar{K}^{*0}K^{*+}$ | 0.56 | 0.12 | 0.19 | 0.21 | 0.44 | 0.28 | 0.08 | 0.83 |
| $D_s^+ \to \bar{K}_1^0(1270)K^+,\ \bar{K}_1^0(1270) \to K^-\rho^+$ | 0.62 | 0.30 | 0.18 | 0.40 | 0.25 | 0.27 | 0.08 | 0.90 |
| $D_s^+ \to \bar{K}_1^0(1270)K^+,\ \bar{K}_1^0(1270)[S] \to \bar{K}^{*0}\pi^0$ | 0.55 | 0.14 | 0.07 | 0.31 | 0.00 | 0.08 | 0.07 | 0.67 |
| $D_s^+ \to \bar{K}_1^0(1270)K^+,\ \bar{K}_1^0(1270)[S] \to K^{*-}\pi^+$ | 0.54 | 0.14 | 0.07 | 0.30 | 0.00 | 0.08 | 0.07 | 0.65 |
| $D_s^+ \to \bar{K}_1^0(1270)K^+,\ \bar{K}_1^0(1270)[S] \to K^*\pi$ | 0.54 | 0.14 | 0.07 | 0.29 | 0.00 | 0.08 | 0.07 | 0.64 |
| $D_s^+ \to \bar{K}_1^0(1270)K^+,\ \bar{K}_1^0(1270)[D] \to \bar{K}^{*0}\pi^0$ | 0.44 | 0.29 | 0.11 | 0.67 | 0.09 | 0.16 | 0.05 | 0.88 |
| $D_s^+ \to \bar{K}_1^0(1270)K^+,\ \bar{K}_1^0(1270)[D] \to K^{*-}\pi^+$ | 0.43 | 0.29 | 0.11 | 0.67 | 0.09 | 0.16 | 0.05 | 0.87 |
| $D_s^+ \to \bar{K}_1^0(1270)K^+,\ \bar{K}_1^0(1270)[D] \to K^*\pi$ | 0.43 | 0.29 | 0.11 | 0.67 | 0.09 | 0.16 | 0.05 | 0.87 |
| $D_s^+ \to \bar{K}_1^0(1270)K^+,\ \bar{K}_1^0(1270) \to K^*\pi$ | 0.71 | 0.32 | 0.16 | 0.71 | 0.08 | 0.21 | 0.10 | 1.10 |
| $D_s^+ \to \bar{K}_1^0(1400)K^+,\ \bar{K}_1^0(1400)[S] \to \bar{K}^{*0}\pi^0$ | 0.76 | 0.21 | 0.27 | 0.49 | 0.36 | 0.44 | 0.09 | 1.12 |
| $D_s^+ \to \bar{K}_1^0(1400)K^+,\ \bar{K}_1^0(1400)[S] \to K^{*-}\pi^+$ | 0.77 | 0.21 | 0.27 | 0.49 | 0.36 | 0.44 | 0.09 | 1.13 |
| $D_s^+ \to \bar{K}_1^0(1400)K^+,\ \bar{K}_1^0(1400)[S] \to K^*\pi$ | 0.76 | 0.21 | 0.27 | 0.49 | 0.36 | 0.44 | 0.09 | 1.12 |
| $D_s^+ \to a_0^0(980)\rho^+$ | 0.74 | 0.28 | 0.27 | 0.30 | 0.29 | 0.47 | 0.06 | 1.05 |
| $D_s^+ \to f_1(1420)\pi^+,\ f_1(1420) \to K^{*-}K^+$ | 0.39 | 0.10 | 0.11 | 0.37 | 0.19 | 0.18 | 0.11 | 0.62 |
| $D_s^+ \to f_1(1420)\pi^+,\ f_1(1420) \to K^{*+}K^-$ | 0.37 | 0.10 | 0.11 | 0.37 | 0.19 | 0.18 | 0.11 | 0.61 |
| $D_s^+ \to f_1(1420)\pi^+,\ f_1(1420) \to K^{*\mp}K^\pm$ | 0.38 | 0.10 | 0.11 | 0.33 | 0.19 | 0.18 | 0.11 | 0.59 |
| $D_s^+ \to f_1(1420)\pi^+,\ f_1(1420) \to a_0^0(980)\pi^0$ | 0.22 | 0.07 | 0.08 | 0.16 | 0.13 | 0.07 | 0.07 | 0.33 |
| $D_s^+ \to \eta(1475)\pi^+,\ \eta(1475) \to a_0^0(980)\pi^0$ | 0.72 | 0.31 | 0.29 | 0.40 | 0.33 | 0.39 | 0.10 | 1.07 |
| $\frac{\mathcal{B}(D_s^+\to\bar{K}_1^0(1270)K^+,\bar{K}_1^0(1270)\to K^{*-}\pi^+)}{\mathcal{B}(D_s^+\to\bar{K}_1^0(1270)K^+,\bar{K}_1^0(1270)\to K^-\rho^+)}$ | 0.75 | 0.39 | 0.19 | 0.65 | 0.14 | 0.25 | 0.08 | 1.13 |

the corresponding statistical uncertainty. For each parameter, 300 pull values are obtained, and the deviation of their average from zero is taken as the systematic uncertainty.

## V. BRANCHING FRACTION MEASUREMENT

To determine the absolute BF of the decay $D_s^+ \to K^-K^+\pi^+\pi^0$, the ST candidates with eight tag modes, as shown in Table III, are reconstructed and studied. Then the DT candidates are obtained by fully reconstructing the tag channels and the signal channel.

The ST yields for each tag mode are given by

$$N_{\rm ST} = 2N_{D_s^+D_s^-}\mathcal{B}_{\rm tag}\varepsilon_{\rm ST}, \tag{30}$$

and the DT yields are given by

$$N_{\rm DT} = 2N_{D_s^+D_s^-}\mathcal{B}_{\rm tag}\mathcal{B}_{\rm sig}\varepsilon_{\rm DT}, \tag{31}$$

where $N_{D_s^+D_s^-}$ is the total number of $D_s^+D_s^-$ pairs produced, $\mathcal{B}_{\rm tag(sig)}$ is the BF of the tag (signal) side, and $\varepsilon_{\rm DT(ST)}$ is the DT (ST) efficiency.

The BF of the signal side is determined by

$$\mathcal{B}_{\rm sig} = \frac{N_{\rm DT}}{\mathcal{B}_{\pi^0\to\gamma\gamma}\sum_i N^i_{\rm ST}\varepsilon^i_{\rm DT}/\varepsilon^i_{\rm ST}}, \tag{32}$$

where the $N_{\rm DT}$ and $N^i_{\rm ST}$ yields are obtained from the data sample, while $\varepsilon^i_{\rm DT}$ and $\varepsilon^i_{\rm ST}$ are obtained from the generic MC samples, where $i$ indicates the tag mode. In particular, $\varepsilon^i_{\rm DT}$ is determined by the amplitude analysis model used in the generic MC samples.

The signal BF $\mathcal{B}_{\rm sig}$ is determined by

$$\mathcal{B}_{\rm sig} = \frac{\sum_n N_{n\rm DT}}{\mathcal{B}_{\pi^0\to\gamma\gamma}\sum_n\sum_i N^i_{n\rm ST}\varepsilon^i_{n\rm DT}/\varepsilon^i_{n\rm ST}}, \tag{33}$$

where $i$ denotes the tag mode and $n$ indicates the data sample at 4.178, 4.189–4.219, or 4.226 GeV. For the numerator, $\sum_n N_{n\rm DT}$, the combined data sample is fitted to obtain the total DT data yield.

### A. Event selection

For the BF measurement, it is necessary to guarantee that the DT sample is a strict subset of the ST sample. Therefore, the ST candidates are selected ahead of the selection of DT candidates. For this measurement, the event selection criteria are relaxed or modified in order to increase the signal yield. Here, the background level does not play as crucial of a role as in the amplitude analysis.

In order to reject the soft pions from $D^*$ decays, all the $\pi$ mesons are required to satisfy $P_\pi > 100$ MeV$/c$, and the $\chi^2$ of the kinematic fit for the $\pi^0 \to \gamma\gamma$ decay must be less than 20. The new criteria for selecting $K_S^0$ are $487 < M_{\pi^+\pi^-} < 511$ (MeV$/c^2$), and that the vertex fit $\chi^2$ must be less than 100.

For the ST selection, if there are multiple candidates for a tag mode, the one with $M_{\rm rec}$ closest to the nominal $M_{D_s^{*\pm}}$ [14] is retained. The $M_{\rm rec}$ windows are given in Table II. If the $D_s^+$ meson and the $D_s^-$ meson can be simultaneously reconstructed as ST in an event, both of them are accepted. After the ST selection, if multiple signal candidates are obtained, the one with average mass $\bar{M}$ $(=(M_{D_s^+}+M_{D_s^-})/2)$ closest to the nominal $M_{D_s^\pm}$ is chosen. $M_{D_s^\pm}$ of every candidate must lie in the interval $[1.87, 2.06]$ GeV$/c^2$, and events with both $M_{\rm rec}$ for the $D_s^+$ meson and $M_{\rm rec}$ for the $D_s^-$ meson smaller than 2.1 GeV are rejected.

### B. Data yields, efficiencies, and BFs

The ST yields are determined from fits to the $M_{D_s^-}$ distributions of data, as shown in Fig. 4. In the fits, an MC-simulated shape convolved with a Gaussian function is used to describe the signal shape of $M_{D_s^-}$ and a second-order polynomial function to describe the combinatorial background. For the tag mode $D_s^- \to K_S^0K^-$, there is some peaking background coming from $D^- \to K_S^0\pi^-$. The shape of this background is taken from the generic MC samples and added to the fit leaving its yield floating. For the tag mode $D_s^- \to \pi^-\eta'$, there is peaking background coming from $D_s^- \to \eta\pi^+\pi^-\pi^-$. The shape and the yield of this background are taken from the generic MC samples and added to the fit. The DT yields are obtained from an unbinned fit to the signal $D_s^+$ mass spectrum of the combined data sample, which is shown in Fig. 5. The number of $D_s^+ \to K^-K^+\pi^+\pi^0$ decays is determined to be $\sum_n N_{n\rm DT} = 4365 \pm 83$. Tables XII–XIV summarize the ST efficiencies, DT efficiencies, and ST yields in data samples at 4.178–4.226 GeV.

Inserting the values of the ST and DT data yields and the ST and DT efficiencies into Eq. (33), the BF of the $D_s^+ \to K^-K^+\pi^+\pi^0$ decay is measured to be

$$\mathcal{B}_{\rm sig} = (5.42 \pm 0.10_{\rm stat})\%. \tag{34}$$

### C. Systematic uncertainties in the BF

The sources of the systematic uncertainties in the BF measurement are considered as follows:

(i) *$K^\pm$ meson and $\pi^\pm$ meson tracking/PID efficiencies*.—The ratios between data and MC efficiencies are weighted by the corresponding momentum spectra of signal MC events. The systematic uncertainties associated with tracking efficiency and PID for each charged particle are both estimated to be 0.5%. The samples used to estimate the uncertainties are mentioned in Sec. IV E.

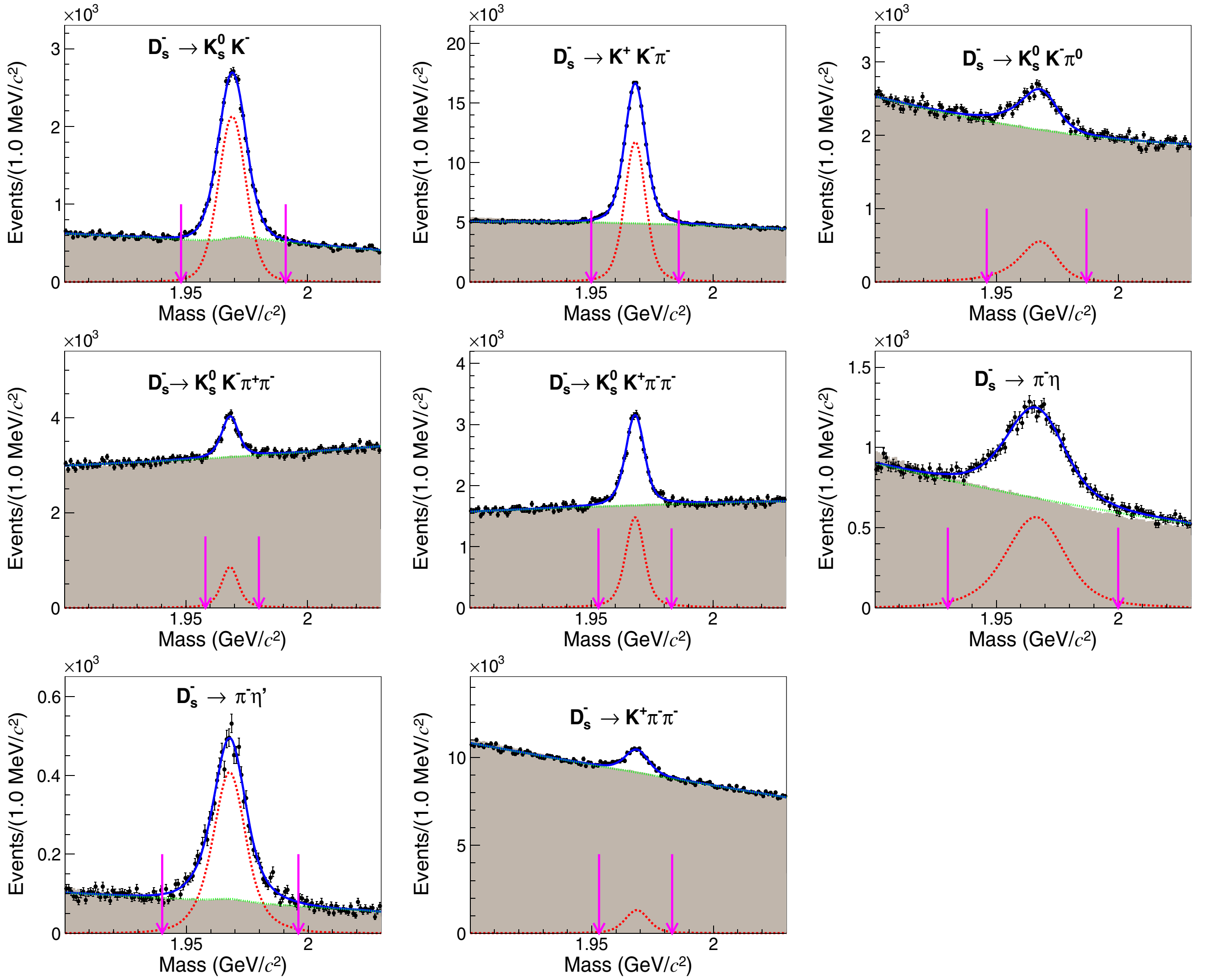


FIG. 4. Fits to the $M_{D_s^-}$ distributions of ST candidates selected from the 4.178 GeV data sample, where the dots with error bars are data, the solid blue curve shows the best fit, the red dotted curve shows the signal shape, the green dashed line shows the shape of the combinatorial backgrounds, the brown area shows the background estimated by the generic MC samples, and the pairs of pink arrows are the mass windows. In the plots for $D_s^- \to K_S^0 K^-$ and $D_s^- \to \pi^- \eta'$ decays, the green dashed lines include contributions from $D^- \to K_S^0 \pi^-$ and $D_s^- \to \eta \pi^+ \pi^- \pi^-$ backgrounds, respectively.

(ii) *$\pi^0$ meson reconstruction efficiency.*—According to the studies in Ref. [52], this systematic uncertainty about the $\pi^0$ reconstruction is assigned to be 2.0%.

(iii) *Numbers of ST $D_s^-$ candidates.*—The BF measurement is not sensitive to systematic uncertainties coming from modifying the polynomial function order, the fit ranges, or the bin sizes. An uncertainty of 0.56% was estimated from alternative fits with different signal shapes. According to Tables XII–XIV, the total ST yield of the eight tag modes is $441684 \pm 1766$, corresponding to the relative statistical uncertainty of 0.40%. The sum of these terms in quadrature is 0.69%.

(iv) *MC statistics.*—The uncertainties of the ST and DT efficiencies are considered, but the DT uncertainties dominate. The uncertainty of the MC statistics is given by $\sqrt{\sum_i f_i (\frac{\delta\epsilon_i}{\epsilon_i})^2}$, where $f_i$ is the tag yield fraction and $\epsilon_i$ is the average DT efficiency of tag mode $i$. The related uncertainty is determined to be 0.34%.

(v) *Shape of the signal $D_s^+$ mass.*—The systematic uncertainty due to the shape of the signal is studied by fitting without the convolved Gaussian function. The difference of the DT yield is taken as the systematic uncertainty and is determined to be 0.5%.

(vi) *Background shape of the signal $D_s^+$ meson.*—For the background shape of the signal $D_s^+$, the MC-simulated shape is used to replace the nominal one, and an uncertainty of 0.75% is obtained.

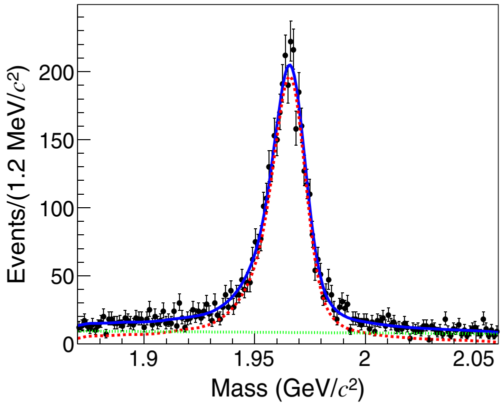


FIG. 5. Invariant mass distribution of the DT $D_s^+ \to K^-K^+\pi^+\pi^0$ events. The black dots with error bars are data. The red dashed line represents the MC-simulated shape convolved with a Gaussian function. The green dashed line represents the MC background shape, which is fitted by a first-order Chebychev polynomial. The blue solid line represents the total fitted shape.

(vii) *Bias of the measurement method*.—Ten updated inclusive generic MC samples are used as fake data to estimate the possible fit bias. The BF for each sample is determined, and the relative difference between the average of BFs and the MC truth value is 0.16%, which is considered negligible.

(viii) *Amplitude model*.—The parameters (magnitudes and phases) of the amplitude model are randomly perturbed 400 times within their statistical uncertainties according to the covariant matrix of the nominal fit to obtain the DT efficiency distribution. Then, the DT efficiency distribution is fitted with a Gaussian function. The fitted width divided by the fitted mean is 0.4% and assigned as the systematic uncertainty arising from the amplitude model.

The systematic uncertainties in the BF are summarized in Table XV. The total systematic uncertainty is obtained by adding them in quadrature. Finally, the BF of the $D_s^+ \to K^-K^+\pi^+\pi^0$ decay is measured to be

$$\mathcal{B}_{\rm sig} = (5.42 \pm 0.10_{\rm stat} \pm 0.17_{\rm syst})\%. \qquad (35)$$

## VI. CONCLUSION

This paper presents the first amplitude analysis of the decay $D_s^+ \to K^-K^+\pi^+\pi^0$. The BF $\mathcal{B}(D_s^+ \to K^-K^+\pi^+\pi^0)$ is measured to be $(5.42 \pm 0.10_{\rm stat} \pm 0.17_{\rm syst})\%$. Using the FFs listed in Table IX and Table XI, the BFs for the intermediate processes are calculated and listed in Table XVI. The $D_s^+ \to \phi\rho^+$ and $D_s^+ \to \bar{K}^{*0}K^{*+}$ decays are found to be dominant, and the decays involving $K_1(1270)$, $K_1(1400)$, $\eta(1475)$, $f_1(1420)$, and $a_0^0(980)$ mesons are also observed with significances larger than $4\sigma$. Compared to the PDG [14] values of $\mathcal{B}(D_s^+ \to K^-K^+\pi^+\pi^0) = (6.3 \pm 0.6)\%$, $\mathcal{B}(D_s^+ \to \phi\rho^+) = (8.4^{+1.9}_{-2.3})\%$, and $\mathcal{B}(D_s^+ \to \bar{K}^{*0}K^{*+}) = (7.2 \pm 2.6)\%$, the absolute BFs $(5.42 \pm 0.10_{\rm stat} \pm 0.17_{\rm syst})\%$, $(5.59 \pm 0.15_{\rm stat} \pm 0.30_{\rm syst})\%$, and $(5.64 \pm 0.23_{\rm stat} \pm 0.27_{\rm syst})\%$

TABLE XII. The efficiencies and ST yields at $E_{\rm cm} = 4.178$ GeV.

| Tag mode | Mass window (GeV/$c^2$) | $N_{\rm ST}$ | $\varepsilon_{\rm ST}(\%)$ | $\varepsilon_{\rm DT}(\%)$ |
|---|---|---|---|---|
| $D_s^- \to K_S^0K^-$ | [1.948, 1.991] | $31668 \pm 315$ | $46.95 \pm 0.07$ | $8.75 \pm 0.09$ |
| $D_s^- \to K^+K^-\pi^-$ | [1.950, 1.986] | $135867 \pm 610$ | $39.00 \pm 0.03$ | $7.09 \pm 0.03$ |
| $D_s^- \to K_S^0K^-\pi^0$ | [1.946, 1.987] | $11284 \pm 512$ | $15.32 \pm 0.11$ | $2.92 \pm 0.05$ |
| $D_s^- \to K_S^0K^-\pi^+\pi^-$ | [1.958, 1.980] | $8032 \pm 273$ | $20.29 \pm 0.12$ | $3.36 \pm 0.07$ |
| $D_s^- \to K_S^0K^+\pi^-\pi^-$ | [1.953, 1.983] | $15645 \pm 289$ | $21.70 \pm 0.06$ | $3.76 \pm 0.05$ |
| $D_s^- \to \pi^-\eta_{\gamma\gamma}$ | [1.930, 2.000] | $18071 \pm 560$ | $43.07 \pm 0.15$ | $7.92 \pm 0.10$ |
| $D_s^- \to \pi^-\eta'_{\pi^+\pi^-\eta_{\gamma\gamma}}$ | [1.940, 1.996] | $7629 \pm 147$ | $18.72 \pm 0.06$ | $3.19 \pm 0.06$ |
| $D_s^- \to K^-\pi^+\pi^-$ | [1.953, 1.983] | $16942 \pm 548$ | $45.80 \pm 0.22$ | $8.39 \pm 0.10$ |

TABLE XIII. The efficiencies and ST yields at $E_{\rm cm} = 4.189$–$4.219$ GeV.

| Tag mode | Mass window (GeV/$c^2$) | $N_{\rm ST}$ | $\varepsilon_{\rm ST}(\%)$ | $\varepsilon_{\rm DT}(\%)$ |
|---|---|---|---|---|
| $D_s^- \to K_S^0K^-$ | [1.948, 1.991] | $18304 \pm 260$ | $46.87 \pm 0.09$ | $9.08 \pm 0.11$ |
| $D_s^- \to K^+K^-\pi^-$ | [1.950, 1.986] | $80417 \pm 508$ | $38.82 \pm 0.04$ | $7.28 \pm 0.04$ |
| $D_s^- \to K_S^0K^-\pi^0$ | [1.946, 1.987] | $6730 \pm 462$ | $14.88 \pm 0.15$ | $3.11 \pm 0.07$ |
| $D_s^- \to K_S^0K^-\pi^+\pi^-$ | [1.958, 1.980] | $5252 \pm 285$ | $20.07 \pm 0.16$ | $3.32 \pm 0.08$ |
| $D_s^- \to K_S^0K^+\pi^-\pi^-$ | [1.953, 1.983] | $8923 \pm 230$ | $21.53 \pm 0.08$ | $3.86 \pm 0.07$ |
| $D_s^- \to \pi^-\eta_{\gamma\gamma}$ | [1.930, 2.000] | $10034 \pm 355$ | $42.37 \pm 0.21$ | $8.15 \pm 0.13$ |
| $D_s^- \to \pi^-\eta'_{\pi^+\pi^-\eta_{\gamma\gamma}}$ | [1.940, 1.996] | $4382 \pm 112$ | $18.66 \pm 0.07$ | $3.45 \pm 0.09$ |
| $D_s^- \to K^-\pi^+\pi^-$ | [1.953, 1.983] | $10051 \pm 529$ | $45.38 \pm 0.30$ | $8.41 \pm 0.13$ |

TABLE XIV. The efficiencies and ST yields at $E_{\mathrm{cm}} = 4.226$ GeV.

| Tag mode | Mass window (GeV/$c^2$) | $N_{\mathrm{ST}}$ | $\epsilon_{\mathrm{ST}}(\%)$ | $\epsilon_{\mathrm{DT}}(\%)$ |
|---|---|---|---|---|
| $D_s^- \to K_S^0 K^-$ | [1.948, 1.991] | $6550 \pm 159$ | $46.42 \pm 0.18$ | $8.81 \pm 0.18$ |
| $D_s^- \to K^+ K^- \pi^-$ | [1.950, 1.986] | $28290 \pm 328$ | $38.27 \pm 0.07$ | $7.30 \pm 0.07$ |
| $D_s^- \to K_S^0 K^- \pi^0$ | [1.946, 1.987] | $2145 \pm 219$ | $15.22 \pm 0.28$ | $2.97 \pm 0.11$ |
| $D_s^- \to K_S^0 K^- \pi^+ \pi^-$ | [1.958, 1.980] | $1708 \pm 217$ | $19.45 \pm 0.30$ | $3.38 \pm 0.14$ |
| $D_s^- \to K_S^0 K^+ \pi^- \pi^-$ | [1.953, 1.983] | $3242 \pm 170$ | $21.31 \pm 0.15$ | $3.90 \pm 0.12$ |
| $D_s^- \to \pi^- \eta_{\gamma\gamma}$ | [1.930, 2.000] | $3699 \pm 244$ | $41.94 \pm 0.40$ | $8.12 \pm 0.22$ |
| $D_s^- \to \pi^- \eta'_{\pi^+\pi^-\eta_{\gamma\gamma}}$ | [1.940, 1.996] | $1646 \pm 75$ | $18.45 \pm 0.13$ | $3.37 \pm 0.14$ |
| $D_s^- \to K^- \pi^+ \pi^-$ | [1.953, 1.983] | $4915 \pm 423$ | $44.75 \pm 0.57$ | $8.41 \pm 0.22$ |

TABLE XV. The systematic uncertainties for the branching fraction measurement.

| Source | Uncertainty (%) |
|---|---|
| Tracking efficiency | 1.5 |
| PID efficiency | 1.5 |
| $\pi^0$ reconstruction efficiency | 2.0 |
| Number of $D_s^-$ | 0.7 |
| MC statistics | 0.3 |
| Signal shape | 0.5 |
| Background shape | 0.8 |
| Amplitude model | 0.4 |
| Total | 32 |

measured in this work have a much better precision. The measurement of $\mathcal{B}(D_s^+ \to \phi\rho^+)$ is consistent with the theory prediction [12] (5.70%), while the measured BF of $D_s^+ \to \bar{K}^{*0} K^{*+}$ decay is still much larger than its prediction (1.5%). The ratio $R_{K_1(1270)} = \frac{\mathcal{B}(K_1^0(1270)\to K^*\pi)}{\mathcal{B}(K_1^0(1270)\to K\rho)}$ mentioned in Table I is determined to be $0.99 \pm 0.15_{\mathrm{stat}} \pm 0.18_{\mathrm{syst}}$ in this analysis. Our result is consistent with the results measured by LHCb [19] and CLEO [20].

## ACKNOWLEDGMENTS

The BESIII Collaboration thanks the staff of BEPCII and the IHEP computing center for their strong support. This work is supported in part by National Key Research and Development Program of China under Contracts No. 2020YFA0406400 and No. 2020YFA0406300; National Natural Science Foundation of China (NSFC) under Contracts No. 11625523, No. 11635010, No. 11735014, No. 11822506, No. 11835012, No. 11935015, No. 11935016, No. 11935018, and No. 11961141012; the Chinese Academy of Sciences (CAS) Large-Scale Scientific Facility Program; Joint Large-Scale Scientific Facility Funds of the NSFC and CAS under Contracts No. U1732263 and No. U1832207; CAS Key Research Program of Frontier Sciences under Contracts No. QYZDJ-SSW-SLH003 and No. QYZDJ-SSW-SLH040; 100 Talents Program of CAS; The Institute of Nuclear and Particle Physics and Shanghai Key Laboratory for Particle Physics and Cosmology; ERC under Contract No. 758462; German Research Foundation DFG under Contract No. 443159800 and Collaborative Research Center Contracts No. CRC 1044, No. FOR 2359, and No. GRK 214; Istituto Nazionale di Fisica Nucleare, Italy; Ministry of Development of Turkey under Contract No. DPT2006K-120470; National Science and Technology fund; Olle Engkvist Foundation under Contract No. 200-0605; STFC (United Kingdom); The Knut and Alice Wallenberg Foundation (Sweden) under Contract No. 2016.0157; The Royal Society (United Kingdom) under Contracts No. DH140054 and No. DH160214; The Swedish Research Council; U.S. Department of Energy under Contracts No. DE-FG02-05ER41374 and No. DE-SC-0012069.

TABLE XVI. The BFs of intermediate processes with final states $K^- K^+ \pi^+ \pi^0$. $K^*\pi$ indicates $\bar{K}^{*0}\pi^0$ and $K^{*-}\pi^+$. For decays with $a_0^0(980)$ in the final state, the quoted BFs include $\mathcal{B}(a_0^0(980) \to K^+ K^-)$. The first and second uncertainties are statistical and systematic, respectively.

| Process | BF (%) |
|---|---|
| $D_s^+[S] \to \phi\rho^+$ | $2.10 \pm 0.09 \pm 0.13$ |
| $D_s^+[P] \to \phi\rho^+$ | $0.52 \pm 0.05 \pm 0.02$ |
| $D_s^+[D] \to \phi\rho^+$ | $0.18 \pm 0.04 \pm 0.02$ |
| $D_s^+ \to \phi\rho^+$ | $2.75 \pm 0.07 \pm 0.15$ |
| $D_s^+[S] \to \bar{K}^{*0} K^{*+}$ | $0.88 \pm 0.05 \pm 0.03$ |
| $D_s^+[P] \to \bar{K}^{*0} K^{*+}$ | $0.37 \pm 0.03 \pm 0.02$ |
| $D_s^+[D] \to \bar{K}^{*0} K^{*+}$ | $0.18 \pm 0.03 \pm 0.01$ |
| $D_s^+ \to \bar{K}^{*0} K^{*+}$ | $1.25 \pm 0.05 \pm 0.06$ |
| $D_s^+ \to \bar{K}_1^0(1270) K^+$, $\bar{K}_1^0(1270) \to K^- \rho^+$ | $0.57 \pm 0.05 \pm 0.04$ |
| $D_s^+ \to \bar{K}_1^0(1270) K^+$, $\bar{K}_1^0(1270)[S] \to K^*\pi$ | $0.21 \pm 0.04 \pm 0.03$ |
| $D_s^+ \to \bar{K}_1^0(1270) K^+$, $\bar{K}_1^0(1270)[D] \to K^*\pi$ | $0.07 \pm 0.02 \pm 0.01$ |
| $D_s^+ \to \bar{K}_1^0(1270) K^+$, $\bar{K}_1^0(1270) \to K^*\pi$ | $0.29 \pm 0.04 \pm 0.04$ |
| $D_s^+ \to \bar{K}_1^0(1400) K^+$, $\bar{K}_1^0(1400) \to K^*\pi$ | $0.44 \pm 0.06 \pm 0.07$ |
| $D_s^+ \to a_0^0(980)\rho^+$ | $0.19 \pm 0.03 \pm 0.03$ |
| $D_s^+ \to f_1(1420)\pi^+$, $f_1(1420) \to K^{*\mp} K^\pm$ | $0.13 \pm 0.02 \pm 0.01$ |
| $D_s^+ \to f_1(1420)\pi^+$, $f_1(1420) \to a_0^0(980)\pi^0$ | $0.04 \pm 0.01 \pm 0.01$ |
| $D_s^+ \to \eta(1475)\pi^+$, $\eta(1475) \to a_0^0(980)\pi^0$ | $0.07 \pm 0.02 \pm 0.02$ |

TABLE XVII. The fixed relations of some amplitudes.

| Index | Amplitude | Relation |
|---|---|---|
| $A_1$ | $D_s^+ \to \bar{K}_1^0(1270)K^+,\ \bar{K}_1^0(1270)[S] \to \bar{K}^{*0}\pi^0$ | |
| $A_2$ | $D_s^+ \to \bar{K}_1^0(1270)K^+,\ \bar{K}_1^0(1270)[S] \to K^{*-}\pi^+$ | |
| $A$ | $D_s^+ \to \bar{K}_1^0(1270)K^+,\ \bar{K}_1^0(1270)[S] \to K^*\pi$ | $A_1 - \sqrt{2} * A_2$ |
| $A_1$ | $D_s^+ \to \bar{K}_1^0(1270)K^+,\ \bar{K}_1^0(1270)[D] \to \bar{K}^{*0}\pi^0$ | |
| $A_2$ | $D_s^+ \to \bar{K}_1^0(1270)K^+,\ \bar{K}_1^0(1270)[D] \to K^{*-}\pi^+$ | |
| $A$ | $D_s^+ \to \bar{K}_1^0(1270)K^+,\ \bar{K}_1^0(1270)[D] \to K^*\pi$ | $A_1 - \sqrt{2} * A_2$ |
| $A_1$ | $D_s^+ \to \bar{K}_1^0(1400)K^+,\ \bar{K}_1^0(1400)[S] \to \bar{K}^{*0}\pi^0$ | |
| $A_2$ | $D_s^+ \to \bar{K}_1^0(1400)K^+,\ \bar{K}_1^0(1400)[S] \to K^{*-}\pi^+$ | |
| $A$ | $D_s^+ \to \bar{K}_1^0(1400)K^+,\ \bar{K}_1^0(1400)[S] \to K^*\pi$ | $A_1 - \sqrt{2} * A_2$ |
| $A_1$ | $D_s^+ \to \eta(1405)\pi^+,\ \eta(1405) \to K^{*-}K^+$ | |
| $A_2$ | $D_s^+ \to \eta(1405)\pi^+,\ \eta(1405) \to K^{*+}K^-$ | |
| $A$ | $D_s^+ \to \eta(1405)\pi^+,\ \eta(1405) \to K^{*\mp}K^\pm$ | $A_1 - A_2$ |
| $A_1$ | $D_s^+ \to f_1(1420)\pi^+,\ f_1(1420) \to K^{*-}K^+$ | |
| $A_2$ | $D_s^+ \to f_1(1420)\pi^+,\ f_1(1420) \to K^{*+}K^-$ | |
| $A$ | $D_s^+ \to f_1(1420)\pi^+,\ f_1(1420) \to K^{*\mp}K^\pm$ | $A_1 - A_2$ [53] |

## APPENDIX A: FIXED RELATIONS OF SOME AMPLITUDES

The amplitudes that are fixed by Clebsch-Gordan coefficients and charge conjugation relations in this analysis are listed in Table XVII. The amplitudes with fixed relation share the same magnitude ($\rho$) and phase ($\phi$).

## APPENDIX B: AMPLITUDES TESTED

Other tested amplitudes which are found to have a significance smaller than $3\sigma$ based on the nominal fit model are listed below:

(1) Cascade amplitudes:
- (a) $D_s^+ \to \bar{K}_1^0(1270)K^+,\ \bar{K}_1^0(1270)[D] \to K^-\rho^+$
- (b) $D_s^+ \to \bar{K}_1^0(1400)K^+,\ \bar{K}_1^0(1400)[D] \to K^*\pi$
- (c) $D_s^+ \to \bar{K}_1^0(1270)K^+,\ \bar{K}_1^0(1270)[P] \to \bar{K}_0^*(1430)\pi$
- (d) $D_s^+ \to \bar{K}_1^0(1400)K^+,\ \bar{K}_1^0(1400)[S,D] \to K^-\rho^+$
- (e) $D_s^+[P] \to \phi(1680)\pi^+,\ \phi(1680)[P] \to K^{*\mp}K^\pm$
- (f) $D_s^+ \to \eta(1405)\pi^+,\ \eta(1405) \to K^{*\mp}K^\pm$
- (g) $D_s^+ \to \eta(1475)\pi^+,\ \eta(1475) \to K^{*\mp}K^\pm$
- (h) $D_s^+ \to \eta(1295)\pi^+,\ \eta(1295) \to a_0^0(980)\pi^0$
- (i) $D_s^+ \to \eta(1405)\pi^+,\ \eta(1405) \to a_0^0(980)\pi^0$
- (j) $D_s^+ \to f_1(1285)\pi^+,\ f_1(1285) \to a_0^0(980)\pi^0$
- (k) $D_s^+ \to f_1(1285)\pi^+,\ f_1(1285) \to K^{*\mp}K^\pm$
- (l) $D_s^+ \to f_1(1510)\pi^+,\ f_1(1510) \to K^{*\mp}K^\pm$

(2) Three-body amplitudes:
- (a) $D_s^+ \to \bar{K}_1^0(1270)K^+,\ \bar{K}_1^0(1270)[P] \to (K\pi)_{\text{S-wave}}\pi$
- (b) $D_s^+[S,P,D] \to (K^-\pi^+)_V K^{*+}$
- (c) $D_s^+[S,P,D] \to \bar{K}^{*0}(K^+\pi^0)_V$
- (d) $D_s^+[S,P,D] \to (K^-K^+)_V\rho^+$
- (e) $D_s^+[S,P,D] \to \phi(\pi^+\pi^0)_V$
- (f) $D_s^+[S,P,D] \to \phi(1680)(\pi^+\pi^0)_V$
- (g) $D_s^+ \to (K^-\rho^+)_A[S,D]K^+$
- (h) $D_s^+ \to (K^*\pi)_A[S,D]K^+$
- (i) $D_s^+ \to (K^-\rho^+)_P K^+$
- (j) $D_s^+ \to (K^-\rho^+)_V K^+$
- (k) $D_s^+ \to (K^{*\mp}K^\pm)_P\pi^+$
- (l) $D_s^+ \to (K^{*\mp}K^\pm)_V\pi^+$
- (m) $D_s^+[P] \to (K^-K^+)_S\rho^+$
- (n) $D_s^+[P] \to \phi(\pi^+\pi^0)_S$
- (o) $D_s^+[P] \to (K^-\pi^+)_S K^{*+}$
- (p) $D_s^+[P] \to \bar{K}^{*0}(K^+\pi^0)_S$
- (q) $D_s^+[P] \to (K^-\pi^+)_{\text{S-wave}}K^{*+}$
- (r) $D_s^+[P] \to \bar{K}^{*0}(K^+\pi^0)_{\text{S-wave}}$
- (s) $D_s^+ \to \eta(1405)\pi^+,\ \eta(1405) \to (K^\mp\pi^0)_V K^\pm$
- (t) $D_s^+ \to \eta(1475)\pi^+,\ \eta(1475) \to (K^\mp\pi^0)_V K^\pm$
- (u) $D_s^+ \to \eta(1405)\pi^+,\ \eta(1405) \to (K^\mp\pi^0)_{\text{S-wave}}K^\pm$
- (v) $D_s^+ \to \eta(1475)\pi^+,\ \eta(1475) \to (K^\mp\pi^0)_{\text{S-wave}}K^\pm$

(3) Four-body nonresonance amplitudes:
- (a) $D_s^+ \to ((K\pi)_{\text{S-wave}}\pi)_A K^+$
- (b) $(K^-(\pi^+\pi^0)_V)_P K^+$
- (c) $(K^-(\pi^+\pi^0)_V)_V K^+$
- (d) $D_s^+ \to ((K^\mp\pi^0)_V K^\pm)_P\pi^+$
- (e) $D_s^+ \to ((K^\mp\pi^0)_V K^\pm)_V\pi^+$
- (f) $((K\pi)_V\pi)_A[S,D]K^+$
- (g) $D_s^+ \to ((\pi^+\pi^0)_V K^-)_A[S,D]K^+$
- (h) $D_s^+[S,P,D] \to (K^-K^+)_V(\pi^+\pi^0)_V$
- (i) $D_s^+[S,P,D] \to (K^-\pi^+)_V(K^+\pi^0)_V$
- (j) $D_s^+ \to (K^-\pi^+)_S(K^+\pi^0)_S$
- (k) $D_s^+ \to (K^-K^+)_S(\pi^+\pi^0)_S$

[1] R. Aaij *et al.* (LHCb Collaboration), J. High Energy Phys. 06 (2012) 115.
[2] M. Ablikim *et al.* (BESIII Collaboration), Phys. Rev. D **99**, 112005 (2019).
[3] J. P. Alexander *et al.* (CLEO Collaboration), Phys. Rev. D **79**, 052001 (2009).
[4] M. Ablikim *et al.* (BESIII Collaboration), Phys. Rev. Lett. **122**, 071802 (2019).
[5] M. Ablikim *et al.* (BESIII Collaboration), Phys. Rev. Lett. **122**, 061801 (2019).
[6] M. Ablikim *et al.* (BESIII Collaboration), Phys. Rev. Lett. **122**, 121801 (2019).
[7] B. Aubert *et al.* (*BABAR* Collaboration), Phys. Rev. Lett. **90**, 242001 (2003).
[8] J. P. Alexander *et al.* (CLEO Collaboration), Phys. Rev. Lett. **100**, 161804 (2008).
[9] P. U. E. Onyisi *et al.* (CLEO Collaboration), Phys. Rev. D **88**, 032009 (2013).
[10] M. Bauer, B. Stech, and M. Wirbel, Z. Phys. C **34**, 103 (1987).
[11] A. N. Kamal, R. C. Verma, and N. Sinha, Phys. Rev. D **43**, 843 (1991).
[12] P. Bedaque, A. Das, and V. S. Mathur, Phys. Rev. D **49**, 269 (1994).
[13] I. Hinchliffe and T. A. Kaeding, Phys. Rev. D **54**, 914 (1996).
[14] M. Tanabashi *et al.* (Particle Data Group), Prog. Theor. Exp. Phys. **2020**, 083C01 (2020).
[15] H. Y. Cheng, Phys. Lett. B **707**, 116 (2012).
[16] P. Avery *et al.* (CLEO Collaboration), Phys. Rev. Lett. **68**, 1279 (1992).
[17] H. Albrecht *et al.* (ARGUS Collaboration), Z. Phys. C **53**, 361 (1992).
[18] P. F. Guo, D. Wang, and F. S. Yu, Nucl. Phys. Rev. **36**, 125 (2019).
[19] R. Aaij *et al.*, J. High Energy Phys. 02 (2019) 126.
[20] M. Artuso *et al.* (CLEO Collaboration), Phys. Rev. D **85**, 122002 (2012).
[21] M. Ablikim *et al.* (BESIII Collaboration), Phys. Rev. D **95**, 072010 (2017).
[22] R. Aaij *et al.* (LHCb Collaboration), Eur. Phys. J. C **78**, 443 (2018).
[23] H. Guler *et al.* (Belle Collaboration), Phys. Rev. D **83**, 032005 (2011).
[24] C. Daum *et al.* (ACCMOR Collaboration), Nucl. Phys. **B187**, 1 (1981).
[25] P. d'Argent, N. Skidmore, J. Benton, J. Dalseno, E. Gersabeck, S. T. Harnew, P. Naik, C. Prouve, and J. Rademacker, J. High Energy Phys. 05 (2017) 143.
[26] B. S. Zou and D. V. Bugg, Eur. Phys. J. A **16**, 537 (2003).
[27] M. Ablikim *et al.* (BESIII Collaboration), Nucl. Instrum. Methods Phys. Res., Sect. A **614**, 345 (2010).
[28] M. Ablikim *et al.* (BESIII Collaboration), Chin. Phys. C **44**, 040001 (2020).
[29] C. H. Yu *et al.*, in *Proceedings of IPAC2016, Busan, Korea* (Joint Accelerator Conferences Website, Geneva, Switzerland, 2016).
[30] X. Li *et al.*, Radiat. Detect. Technol. Methods **1**, 13 (2017).
[31] Y. X. Guo *et al.*, Radiat. Detect. Technol. Methods **1**, 15 (2017).
[32] J. Adler *et al.* (MARK III Collaboration), Phys. Rev. Lett. **60**, 89 (1988).
[33] S. Agostinelli *et al.* (GEANT4 Collaboration), Nucl. Instrum. Methods Phys. Res., Sect. A **506**, 250 (2003).
[34] Z. Y. Deng *et al.*, Chin. Phys. C **30**, 371 (2006), http://hepnp.ihep.ac.cn/article/id/283d17c0-e8fa-4ad7-bfe3-92095466def1.
[35] R. G. Ping, Chin. Phys. C **38**, 083001 (2014).
[36] R. G. Ping, Chin. Phys. C **32**, 599 (2008); D. J. Lange, Nucl. Instrum. Methods Phys. Res., Sect. A **462**, 152 (2001).
[37] S. Jadach, B. F. L. Ward, and Z. Was, Phys. Rev. D **63**, 113009 (2001).
[38] P. Golonka and Z. Was, Eur. Phys. J. C **45**, 97 (2006).
[39] J. C. Chen, G. S. Huang, X. R. Qi, D. H. Zhang, and Y. S. Zhu, Phys. Rev. D **62**, 034003 (2000).
[40] M. Xu *et al.*, Chin. Phys. C **33**, 428 (2009).
[41] S. U. Chung, Phys. Rev. D **48**, 1225 (1993).
[42] S. U. Chung, Phys. Rev. D **57**, 431 (1998).
[43] F. von Hippel and C. Quigg, Phys. Rev. D **5**, 624 (1972).
[44] K. Cranmer, Comput. Phys. Commun. **136**, 198 (2001).
[45] W. Verkerke and D. P. Kirkby, RooFit Users Manual **v2**, 07 (2006), http://roofit.sourceforge.net/.
[46] M. Ablikim *et al.* (BESIII Collaboration), Phys. Rev. D **95**, 072010 (2017).
[47] H. Guler *et al.* (Belle Collaboration), Phys. Rev. D **83**, 032005 (2011).
[48] G. J. Gounaris and J. J. Sakurai, Phys. Rev. Lett. **21**, 244 (1968).
[49] S. M. Flatté, Phys. Lett. **63B**, 224 (1976).
[50] M. Ablikim *et al.* (BESIII Collaboration), Phys. Rev. D **95**, 032002 (2017).
[51] I. Adachi *et al.* (*BABAR* and Belle Collaborations), Phys. Rev. D **98**, 112012 (2018).
[52] M. Ablikim *et al.* (BESIII Collaboration), Phys. Rev. D **99**, 091101(R) (2019).
[53] F. K. Guo, C. Hanhart, U.-G. Meißner, Q. Wang, Q. Zhao, and B.-S. Zou, Rev. Mod. Phys. **90**, 015004 (2018).